Quarterly Technical Report

Solid State Research

2004:4

Lincoln Laboratory
MASSACHUSETTS INSTITUTE OF TECHNOLOGY
Lexington, Massachusetts
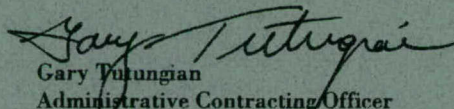
The ESC Public Affairs Office has reviewed this report, and it is releasable to the National Technical Information Service, where it will be available to the general public, including foreign nationals.

This technical report has been reviewed and is approved for publication.

FOR THE COMMANDER

Gary Tutungian
Administrative Contracting Officer
Plans and Programs Directorate
Contracted Support Management

Massachusetts Institute of Technology
Lincoln Laboratory

Solid State Research

Quarterly Technical Report
2004:4

1 August – 31 October 2004

Issued 12 May 2005

Lexington   Massachusetts

ABSTRACT

This report covers in detail the research work of the Solid State Division at Lincoln Laboratory for the period 1 August through 31 October 2004. The topics covered are Quantum Electronics, Electro-optical Materials and Devices, Submicrometer Technology, Biosensor and Molecular Technologies, Advanced Imaging Technology, Analog Device Technology, and Advanced Silicon Technology. Funding is provided by several DoD organizations—including the Air Force, Army, DARPA, MDA, Navy, NSA, and OSD—and also by the DOE, NASA, and NIST.

TABLE OF CONTENTS

7. ADVANCED SILICON TECHNOLOGY

LIST OF ILLUSTRATIONS

LIST OF ILLUSTRATIONS (Continued)

LIST OF TABLES

INTRODUCTION

1. QUANTUM ELECTRONICS

A wavelength tuning range $\Delta\lambda = 0.4$ μm, at a center wavelength ~3.7 μm, has been demonstrated from an optically pumped, GaSb-based semiconductor laser grown on a GaSb substrate when placed in a Littrow external cavity. The peak single-facet output power was 1.2 W with a corresponding linewidth of <10 GHz; when the laser element was placed in a Littman-Metcalf cavity, a narrower linewidth of <5 GHz was achieved at the expense of a smaller tuning range of $\Delta\lambda = 0.27$ μm and lower peak output power of 0.4 W.

2. ELECTRO-OPTICAL MATERIALS AND DEVICES

Extremely low surface recombination velocity as low as 30 cm/s has been achieved for 0.53-eV GaInAsSb/AlGaAsSb double heterostructures grown by organometallic vapor phase epitaxy. This value was determined from minority carrier lifetime measurements by photoluminescence decay, and is over an order of magnitude lower than values reported previously.

3. SUBMICROMETER TECHNOLOGY

Numerical simulations of the impact of bubbles on liquid immersion lithography have shown that the greatest effect is due to bubbles close to the resist surface. Beyond several bubble diameters the impact of a bubble was shown to be negligible.

An experimental evaluation of the effects of surfactants on patterning quality for liquid immersion lithography at 193-nm wavelength was conducted using a contact phase shift photomask. Measurements of line edge roughness revealed no negative effects due to the surfactants.

4. BIOSENSOR AND MOLECULAR TECHNOLOGIES

The Affinity Magnet (AM) protocol has been incorporated into three versions of a field-portable cartridge, with all required reagents and components contained within the cartridges. The three versions are a two-valve cartridge consisting of modified commercial off-the-shelf (COTS) components, a single-valve version using a custom design, and a single-valve cartridge using a COTS valve as the main element.

5. ADVANCED IMAGING TECHNOLOGY

The first prototype devices of a new charge-coupled device (CCD) architecture for adaptive imaging in ground-based astronomy called the orthogonal-transfer array (OTA) have been successfully tested. The initial characterization has focused on small OTAs consisting of 2 × 2 arrays of OTCCD cells and have confirmed the correct operation of the addressing and control logic as well as the OTCCD cells.

6. ANALOG DEVICE TECHNOLOGY

A novel digital compensation technique has been applied to linearize the generation of a multigigahertz chirp. This approach combines recently available commercial high-speed digital, mixed-signal, and analog integrated circuits along with microwave components to create a 15.5–24-GHz chirp over 60 ns with <0.4% nonlinearity.

7. ADVANCED SILICON TECHNOLOGY

Alignment data obtained from wafers aligned and bonded in our facility have been analyzed. An advanced wafer alignment tool currently under development is described.

REPORTS ON SOLID STATE RESEARCH
1 AUGUST THROUGH 31 OCTOBER 2004

PUBLICATIONS

Two-Dimensional Angular Optical Scattering Patterns of Microdroplets in the Mid Infrared with Strong and Weak Absorption	K. B. Aptowicz* Y.-L. Pan* R. K. Chang* R. G. Pinnick* S. C. Hill* R. L. Tober* A. K. Goyal T. H. Jeys B. V. Bronk*	*Opt. Lett.* **29**, 1965 (2004)
Three-Dimensional Imaging with Arrays of Geiger-Mode Avalanche Photodiodes	B. F. Aull A. H. Loomis D. J. Young A. Stern B. J. Felton P. J. Daniels D. J. Landers L. Retherford D. D. Rathman R. M. Heinrichs R. M. Marino	*Proc. SPIE* **5353**, 105 (2004)
Quantum Computing with Superconductors	K. K. Berggren	*Proc. IEEE* **92**, 1630 (2004)

---

*Author not at Lincoln Laboratory.

---

*Author not at Lincoln Laboratory.

Electron Mobility in Very Low Density GaN/AlGaN/GaN Heterostructures	M. J. Manfra K. W. Baldwin* A. M. Sergent* R. J. Molnar J. M. Caissie	*Appl. Phys. Lett.* **85**, 1722 (2004)
Probing Decoherence with Electromagnetically Induced Transparency in Superconductivity Quantum Circuits	K. M. V. Murali* Z. Dutton* W. D. Oliver D. S. Crankshaw T. P. Orlando*	*Phys. Rev. Lett.* **93**, 87003-1 (2004)
165-W Cryogenically Cooled Yb:YAG Laser	D. J. Ripin J. R. Ocha R. L. Aggarwal T. Y. Fan	*Opt. Lett.* **29**, 2154 (2004)
Scattering in Liquid Immersion Lithography	M. Switkes T. M. Bloomstein R. R. Kunz M. Rothschild J. W. Ruberti* T. A. Shedd* M. Yeung*	*Proc. SPIE* **5377**, 469 (2004)

PRESENTATIONS[†]

Quasi-bulk GaN by HVPE	R. J. Molnar J. Caissie A. Loomis M. J. Manfra	ONR Electronic Materials Program Review, Monterey, California, 1-4 August 2004
An Angle-Resolved Scatterometer in the VUV Using an Apodized Pupil Function	T. M. Bloomstein D. E. Hardy M. Rothschild	International Symposium on Immersion and 157 nm Lithography, Vancouver, Canada, 2-5 August 2004

---

*Author not at Lincoln Laboratory.

[†] Titles of presentations are listed for information only. No copies are available for distribution.

Development of a 193 nm Based Diffractometer for Advanced Photomask Characterization	T. M. Bloomstein D. E. Hardy M. Rothschild A. Grenville*	International Symposium on Immersion and 157 nm Lithography, Vancouver, Canada, 2-5 August 2004
Controlled Contamination Studies in 193-nm Immersion Lithography	V. Liberman S. T. Palmacci D. E. Hardy M. Rothschild A. Grenville*	International Symposium on Immersion and 157 nm Lithography, Vancouver, Canada, 2-5 August 2004
Laser-Induced Birefringence in Modified Fused Silica: 157-nm and 193-nm Irradiation	V. Liberman M. Rothschild S. T. Palmacci D. E. Hardy A. Grenville*	International Symposium on Immersion and 157 nm Lithography, Vancouver, Canada, 2-5 August 2004
Long-Term 193-nm Laser Irradiation of Thin-Film-Coated CaF_2 in the Presence of H_2O	V. Liberman M. Switkes M. Rothschild S. T. Palmacci J. H. C. Sedlacek A. Grenville*	International Symposium on Immersion and 157 nm Lithography, Vancouver, Canada, 2-5 August 2004
First Patterning Results with a 157 nm Immersion Microstepper	M. Switkes T. Bloomstein M. Rothschild K. J. Orvek* E. Arriola* T. Morrison*	International Symposium on Immersion and 157 nm Lithography, Vancouver, Canada, 2-5 August 2004
Bubbles in Immersion Lithography	M. Switkes M. Rothschild J. W. Ruberti* T. A. Shedd*	International Symposium on Immersion and 157 nm Lithography, Vancouver, Canada, 2-5 August 2004

*Author not at Lincoln Laboratory.

HTS Film for High-Power Microwave Applications	D. Oates	Air Force Office of Scientific Research Annual Review, Morgantown, West Virginia, 3-6 August 2004
CANARY B-Cell Sensor for Rapid, Sensitive Identification of Pathogens	J. Harper M. Petrovick F. Nargi E. Schwoebel T. Rider	Lincoln Laboratory Technical Seminar Series, University of Connecticut, Storrs, Connecticut, 23 September 2004
Optically Patterned Deep-Submicron Josephson Junctions for Quantum Computation	B. Cord* V. Bolkovsky E. Macedo W. D. Oliver T. P. Orlando* K. K. Berggren*	Applied Superconductivity Conference, Jacksonville, Florida, 3-8 October 2004
Microwave Properties of MgB_2 Thin Films Grown by Reactive Evaporation	D. Oates	Applied Superconductivity Conference, Jacksonville, Florida, 3-8 October 2004
Temperature Dependence of Intermodulation Distortion in YBCO: Understanding Nonlinearity	D. Oates S.-H. Park D. Agassi* G. Koren* K. Irgmeier*	Applied Superconductivity Conference, Jacksonville, Florida, 3-8 October 2004
Optimization of the Nonlinear Microwave Response of YBaCuO Films on MgO Substrates	D. E. Oates D. Seron* S. H. Park M. A. Hein* P. J. Hirst* R. G. Humphries*	Applied Superconductivity Conference, Jacksonville, Florida, 3-8 October 2004

---

*Author not at Lincoln Laboratory.

Resonant Readout of a Persistent-Current Qubit with SQUID Josephson Inductance	W. Oliver J. C. Lee K. Berggren* T. Orlando*	Applied Superconductivity Conference, Jacksonville, Florida, 3-8 October 2004
Spectroscopy on a Superconducting Persistent-Current Qubit	W. Oliver T. P. Orlando* Y. Yu* D. Nakada*	Applied Superconductivity Conference, Jacksonville, Florida, 3-8 October 2004
Energy Relaxation Time Between Macroscopic Quantum Levels in a Supercondoucting Persistent-Current Qubit	W. Oliver T. P. Orlando* Y. Yu* D. Nakada* J. C. Lee* D. Crankshaw* K. K. Berggren*	Applied Superconductivity Conference, Jacksonville, Florida, 3-8 October 2004
DC and RF Characterization of Fully-Depleted SOI and Strained SOI MOSFETs	C.-L. Chen P. W. Wyatt C. L. Keast C. K. Chen D. R. Yost M. Fritze R. Lambert	IEEE International SOI Conference, Charlestown, South Carolina, 4-7 October 2004
Demonstration of Charge-Coupled Devices in Fully Depleted SOI	J. Sage V. Bolkhovsky W. Oliver D. Santiago T. Weir	IEEE International SOI Conference, Charlestown, South Carolina, 4-7 October 2004
An Investigation of Wafer-to-Wafer Alignment Tolerances for Three-Dimensional Integrated Circuit Fabrication	K. Warner C. Keast R. D'Onofrio C. K. Chen S. Poesse	IEEE International SOI Conference, Charlestown, South Carolina, 4-7 October 2004

---

*Author not at Lincoln Laboratory.

Optical Techniques for Bioaerosol Detection	J. D. Hybl	Optical Science and Engineering Program Seminar, University of Colorado, Boulder, Colorado, 18 October 2004
Laser-Induced Breakdown Spectroscopy of Airborne Bioaerosol Particles	J. D. Hybl S. Tysk	SPIE European Symposium on Optics and Photonics for Defence and Security, London, UK, 25-28 October 2004
DARPA Chemical and Biological Sensor Standards Study	T. H. Jeys	SPIE European Symposium on Optics and Photonics for Defence and Security, London, UK, 25-28 October 2004
Ultraviolet LED-Based Biological Agent Sensor and Trigger	T. H. Jeys L. Desmarais J. Ingwersen X. T. Le V. Daneu	SPIE European Symposium on Optics and Photonics for Defence and Security, London, UK, 25-28 October 2004
Compact Solid-State Sources and Their Applications	J. J. Zayhowski	SPIE European Symposium on Optics and Photonics for Defence and Security, London, UK, 25-28 October 2004
Arrays of InP-Based Geiger-Mode APDs	K. A. McIntosh	SPIE International Symposium: Optics East, Philadelphia, Pennsylvania, 25-28 October 2004
Measurement of Thermo-optic Properties of $AgGaSe_2$ in the 300–100 K Range	R. L. Aggarwal	6th Joint Conference on Standoff Detection for Chemical and Biological Defense, Williamsburg, Virginia, 25-29 October 2004

ORGANIZATION

SOLID STATE DIVISION

D. C. Shaver, Head
R. W. Ralston, Associate Head
N. L. DeMeo, Jr., Assistant
Z. J. Lemnios, Senior Staff
K. J. Challberg, Administrative Staff
L. K. Pacheco, Administrative Staff
J. D. Pendergast, Administrative Staff

SUBMICROMETER TECHNOLOGY

M. Rothschild, Leader
T. M. Lyszczarz, Assistant Leader
T. H. Fedynyshyn, Senior Staff
R. R. Kunz, Senior Staff

Astolfi, D. K.	Liberman, V.
Bloomstein, T. M.	Palmacci, S. T.
Cann, S. G.	Pottebaum, I. S.
Efremow, N. N., Jr.	Sedlacek, J. H. C.
Geis, M. W.	Spector, S. J.
Goodman, R. B.	Switkes, M.
Krohn, K. E.	Wynn, C. M.
Leibowitz, F. L.	Yoon, J. U.
Lennon, D. M.	

QUANTUM ELECTRONICS

A. Sanchez-Rubio, Leader
T. Y. Fan, Assistant Leader
T. H. Jeys, Senior Staff
J. J. Zayhowski, Senior Staff

Aggarwal, R. L.	Hybl, J. D.
Augst, S. J.	Lynch, E. J.
Chann, B.	O'Brien, P. W.
Daneu, J. L.	Ochoa, J. R.
DiNatale, W. F.	Ranka, J. K.
Eapen, X. L.	Ripin, D. J.
Goyal, A. K.	Tysk, S. M.
Herzog, W. D.	

ELECTRO-OPTICAL MATERIALS AND DEVICES

J. C. Twichell, Leader
G. W. Turner, Assistant Leader
S. Verghese, Assistant Leader
J. P. Donnelly, Senior Staff
D. L. Spears, Senior Staff
C. A. Wang, Senior Staff
R. C. Williamson, Senior Staff

Bailey, R. J.	Huang, R. K.	Missaggia, L. J.
Calawa, D. R.	Jensen, K. E.	Molnar, R. J.
Calawa, S. D.	Juodawlkis, P. W.	Mull, D. E.
Connors, M. K.	LaForge, B. E.	Napoleone, A.
Duerr, E. K.	Liau, Z. L.	Nitishin, P. M.
Goodhue, W. D.	Mahan, J. M.	Oakley, D. C.
Groves, S. H.	Mahoney, L. J.	O'Donnell, F. J.
Hargreaves, J. J.	Manfra, M. J.	Plant, J. J.
Harman, T. C.	McIntosh, K. A.	Swint, R. B.
Harris, C. T.	McNulty, D. D.	Younger, R. D.

1. QUANTUM ELECTRONICS

1.1 WAVELENGTH TUNING OVER $\lambda = 3.5$–3.9 μm FROM AN OPTICALLY PUMPED, GaSb-BASED, SEMICONDUCTOR LASER

Wide wavelength tunability from mid-infrared laser sources operating in the range $\lambda = 3$–5 μm is of interest for both commercial and military applications. For chemical sensing applications, narrow linewidth operation is also required. Here, we report on wavelength tuning characteristics of GaSb-based, optically pumped semiconductor lasers (OPSLs). The results expand upon those presented in a previous report [1]. By refining the external cavity configuration, we have been able to achieve a tuning range >0.4 μm with a laser linewidth <10 GHz.

The OPSL structure was based on the aluminum-free, integrated-absorber design [2]–[4]. The laser structure was grown by solid-source molecular beam epitaxy on a (100) n-GaSb substrate. Ten equally spaced type-II "W" quantum wells, each consisting of 21-Å InAs/24-Å InGaSb/21-Å InAs, were embedded within the 1-μm-thick $Ga_{0.85}In_{0.15}As_{0.08}Sb_{0.92}$ integrated absorber. A 4-μm-thick GaSb cap layer served as the top optical cladding while the GaSb substrate served as the lower cladding. No aluminum was used in the growth of this laser structure. The laser sample was cleaved to create 2-mm-long lasers and mounted epi-side-down using In solder. Lasers were cooled in a liquid-nitrogen dewar and optically pumped using a $\lambda = 1.8$ μm InGaAs/InP diode laser array operating quasi-cw (100 μs, 250 Hz). The fast-axis far-field divergence from the OPSL was measured to be 30° full width at half-maximum (FWHM). The peak power emitted per facet was measured to be 1.35 W at a pump power of 24 W. The free-running laser wavelength was 3.87 μm with a spectral width of 0.04 μm FWHM. A two-layer antireflection coating consisting of Al_2O_3 and TiO_2 was then applied to the output facet while the rear facet remained uncoated. This suppressed lasing from the device up to the highest pump power available.

The device was first placed in the Littrow external cavity depicted in Figure 1-1. The emission in the fast axis was collimated using an $f = 25$ mm ZnSe asphere. An $f = -1250$ mm CaF_2 cylindrical lens having
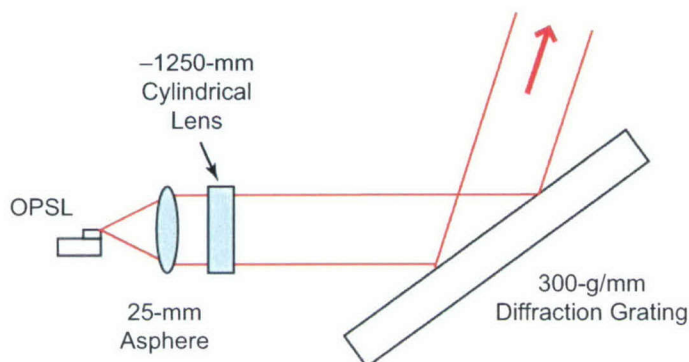
Figure 1-1. Littrow external cavity configuration.

1
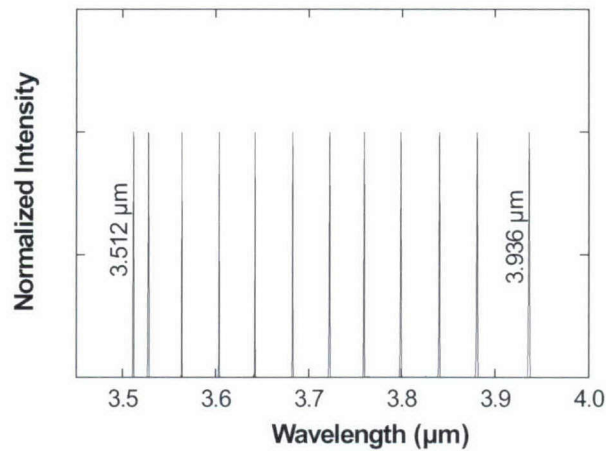
Figure 1-2. Normalized laser spectra as wavelength is tuned using the Littrow external cavity. Laser was operated at 78 K and optically pumped at λ = 1.8 μm under quasi-cw conditions.

power in the slow axis was used to partially compensate for the laser beam astigmatism. The first-order diffracted beam from the 300-g/mm grating dispersed radiation along the fast axis of the optical mode with a diffraction efficiency of ~35%. This grating diffraction efficiency represents an upper bound to the feedback level because additional losses are incurred in coupling from free space back into the laser mode. The output beam was taken from the zero-order grating reflection. The calculated spectral bandwidth of the feedback (FW1/e^2 of coupling efficiency) is <20 GHz over the wavelength range of interest. Figure 1-2 plots a series of spectra taken as the laser wavelength is tuned by rotating the diffraction grating. The laser spectra were taken using a grating spectrometer in combination with a boxcar integrator set to a delay of 25 μs with respect to the leading edge of the pump pulse. The amplitude of each spectrum is normalized. The lasing wavelength was tuned over 0.424 μm from 3.512 to 3.936 μm. Throughout the tuning range the side-mode suppression ratio was greater than our noise floor of >25 dB. Figure 1-3 plots the peak output power and threshold pump power as a function of wavelength. The peak output power is 1.2 W at λ = 3.84 μm. A peak power of >0.5 W is obtained over a tuning range of 0.25 μm. At long wavelengths the threshold pump power is <1 W. It was not possible to observe the expected increase in threshold at the long wavelength limit of the tuning range because of a thermally induced shift in bandgap. The tuning range towards shorter wavelengths is determined by a combination of thermal broadening, band filling, and inhomogeneous broadening within the quantum well gain region. Figure 1-4 plots the laser linewidth as measured using a scanning Fabry-Perot interferometer. At conditions corresponding to the maximum achieved output power, a laser linewidth of 8.9 GHz was measured. As expected, this is roughly one half of the calculated FW1/e^2 feedback bandwidth.

In an effort to further narrow the laser linewidth, the OPSL was placed in the Littman-Metcalf external cavity shown in Figure 1-5. In addition to the optics used before, a gold-coated mirror reflects the
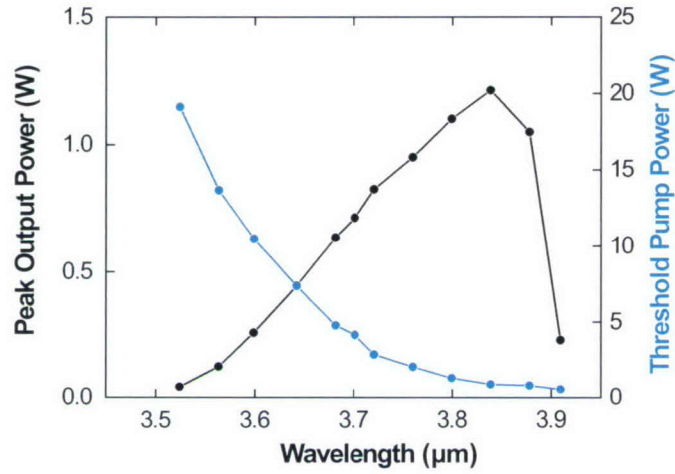
Figure 1-3. Output power and threshold pump power as a function of wavelength as the optically pumped semiconductor laser (OPSL) is tuned using the Littrow external cavity. Laser was operated at 78 K and optically pumped at λ = 1.8 μm under quasi-cw conditions. A peak output power of 1.2 W occurs at λ = 3.84 μm.
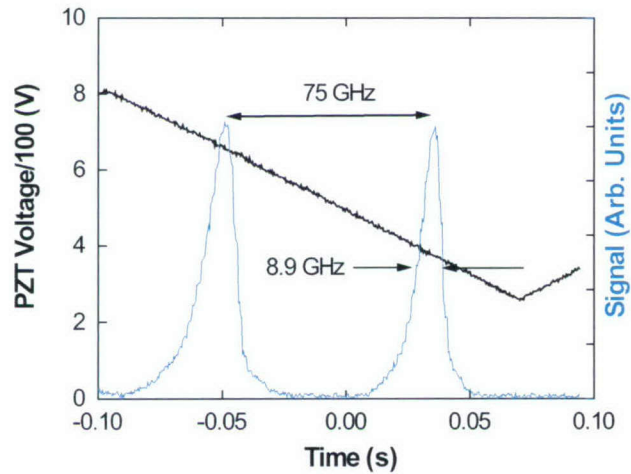
Figure 1-4. Laser linewidth of 8.9 GHz at a center wavelength of λ = 3.839 μm is measured using a Fabry-Perot interferometer under conditions yielding a peak output power of ~1.2 W.

3
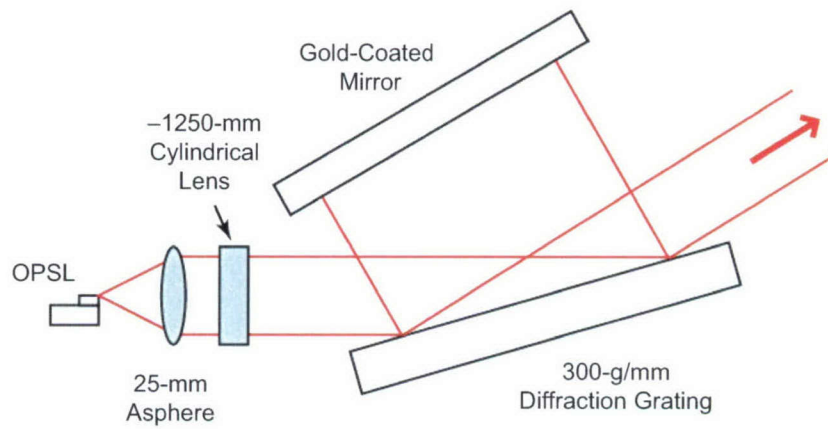
Figure 1-5. Littman-Metcalf external cavity configuration.
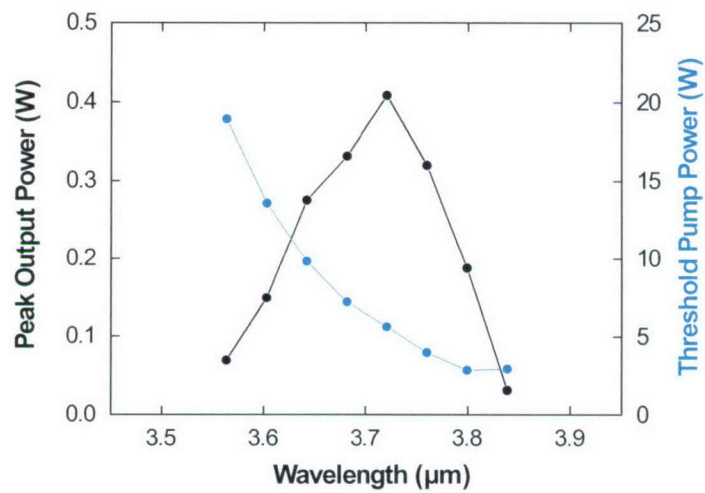
Figure 1-6. Output power and threshold pump power as a function of wavelength as the OPSL is tuned using the Littman-Metcalf external cavity. A peak output power of 0.4 W occurs at $\lambda = 3.72$ μm.
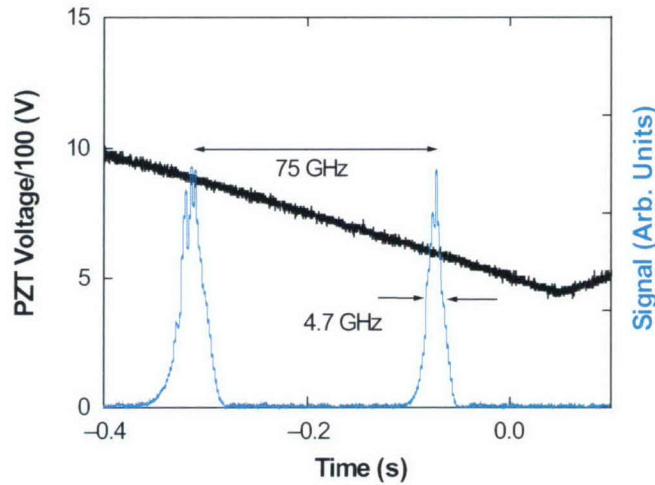
Figure 1-7. Laser linewidth measured using a scanning Fabry-Perot interferometer at a center wavelength of λ = 3.799 μm. At the maximum output power of 0.4 W, the measured laser linewidth is 4.7 GHz.

first-order diffracted beam from the grating back onto itself. The laser wavelength is tuned by rotating this mirror. As before, the zero-order grating reflection provides the output. By double-passing the diffraction grating, the dispersion is roughly doubled such that the feedback bandwidth is <10 GHz. At the angle of incidence used in the experiments ($\theta_i = 21°$), the diffraction efficiency is about 25%. Since the laser beam double-passes the grating, the maximum obtainable feedback is $(0.25)^2 = 0.06$. As shown in Figure 1-6, the maximum output power was 0.4 W at $\lambda = 3.72$ μm. A tuning range of 0.275 μm was obtained. The minimum threshold pump power was ~3 W. Both the higher threshold and reduced tuning range are attributed to the decreased feedback level. It is unclear, however, why the output power is lower as compared to the Littrow cavity since the threshold pump power has not increased appreciably. The high-resolution Fabry-Perot spectrum in Figure 1-7 shows that the laser linewidth does indeed narrow. A linewidth of 4.7 GHz was measured at a peak output power of 0.4 W.

Thus, we have demonstrated that an aluminum-free OPSL can be tuned over a very wide wavelength range with good efficiency by using standard external cavity techniques. The laser linewidth is well predicted given the geometry of the external cavity.

A. K. Goyal   G. W. Turner
A. Sanchez   M. J. Manfra
P. J. Foti   P. O'Brien

REFERENCES

1. Solid State Research Report, Lincoln Laboratory, MIT, 2003:3, p. 1.

2. H. K. Choi, A. K. Goyal, S. C. Buchter, G. W. Turner, M. J. Manfra, and S. D. Calawa, *Conference on Lasers and Electro-Optics: Technical Digest* (Optical Society of America, Washington, DC, 2000).

3. A. K. Goyal, G. W. Turner, M. J. Manfra, P. J. Foti, P. O'Brien, and A. Sanchez, *2001 IEEE/LEOS Annual Meeting Conference Proceedings* (IEEE, Piscataway, NJ, 2001), p. 200.

4. R. Kaspi, A. Ongstad, G. C. Dente, J. Chavez, M. L. Tilton, and D. Gianardi, *Appl. Phys. Lett.* **81**, 406 (2002).

2. ELECTRO-OPTICAL MATERIALS AND DEVICES

2.1 EXTREMELY LOW SURFACE RECOMBINATION VELOCITY IN GaInAsSb/AlGaAsSb HETEROSTRUCTURES

The performance of minority carrier devices such as light-emitting diodes, photovoltaics, and heterojunction bipolar transistors is sensitive to nonradiative recombination at heterointerfaces, and numerous studies aimed at minimizing surface recombination velocity (SRV) have been reported for heterostructures comprising GaAs- and InP-based III-V alloys [1]. More recently, III-V materials based on GaSb are being developed for optoelectronic devices operating in the mid-infrared wavelength range [2]. For example, GaInAsSb/GaSb and GaInAsSb/AlGaAsSb heterostructures are of particular interest since these alloys show great potential for thermophotovoltaic (TPV) devices used to generate power from a thermal source [3]. It was reported that both GaSb and AlGaAsSb window layers are effective in reducing GaInAsSb SRV [4],[5], and either of these layers can be used to improve device performance of GaInAsSb TPV cells.

From both band-structure considerations and experimental results, however, there appears to be an advantage of AlGaAsSb over GaSb as the window layer. The SRV of p-GaInAsSb doubly capped with p-AlGaAsSb layers was reported to be 720 cm/s compared to 1140 cm/s for GaSb [6]. This lower value was attributed to a more advantageous band alignment between GaInAsSb and AlGaAsSb. The valence band offset between 0.53-eV $Ga_{0.84}In_{0.16}As_{0.14}Sb_{0.86}$ and 1-eV $Al_{0.25}Ga_{0.75}As_{0.02}Sb_{0.98}$ is almost zero, while the GaInAsSb/GaSb interface is a staggered type-II band alignment. The former alignment minimizes carrier trapping at the heterointerface, and consequently these heterostructures should have a comparatively lower SRV, as was observed [6].

While previously reported SRV values of ~720 cm/s are reasonably low [6],[7], significantly better values of over an order of magnitude lower have been reported for GaAs-based materials [1]. This work reports high interfacial quality of GaInAsSb/(Al)Ga(As)Sb double heterostructures (DHs) and the achievement of SRV as low as 30 cm/s. This was achieved by optimizing the heterointerface growth switching sequence, which is particularly critical for Sb-containing alloys [8]–[12].

p-AlGaAsSb/p-GaInAsSb/p-AlGaAsSb DHs with varying GaInAsSb thicknesses were grown by organometallic vapor phase epitaxy with trimethylindium, triethylgallium, tritertiarybutylaluminum, tertiarybutylarsine, and trimethylantimony (TMSb) as organometallic precursors, and dimethylzinc as the p-type doping source [13]–[15]. The layers were nominally lattice matched to (001) GaSb miscut 6° toward (1-11)B and the growth temperature was 525°C. The layer structure, schematically shown in Figure 2-1, consists of a 0.1-μm p-GaSb buffer, 0.02-μm p-AlGaAsSb, p-GaInAsSb (thickness varied), 0.02-μm p-AlGaAsSb, and 0.025-μm p-GaSb. The p-GaInAsSb active layer was doped at 2×10^{17} cm^{-3}, and GaInAsSb thickness was varied from 0.15 to 0.4 μm. The alloy composition of GaInAsSb corresponds to a 300-K photoluminescence (PL) peak emission at about 2.3 μm (0.53 eV). In contrast to previous reports

7
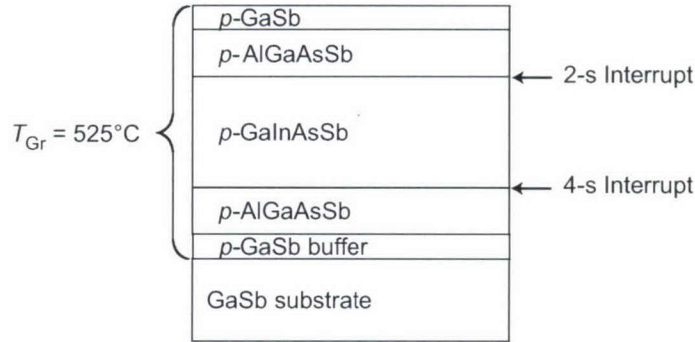
Figure 2-1. Schematic AlGaAsSb/GaInAsSb/AlGaAsSb double heterostructure for measurement of minority carrier lifetime.

[6],[7], AlGa(As)Sb was grown at 525°C, even though the morphology of AlGa(As)Sb was reported to be better when grown at 550°C [15]. The lower temperature of 525°C allows the interruption time between GaInAsSb and AlGaAsSb layers to be minimal (2–4 s) compared to that when GaInAsSb and AlGaAsSb layers are grown at 525 and 550°C, respectively, since temperature changes cannot be made instantaneously. The V/III ratio was 4.4, which is greater than the V/III ratio of 3.2–3.4 for AlGaAsSb grown at 550°C [15]. Two sets of DHs were grown with different Al content in AlGaAsSb. The Al is 0.2 or 0.25, which yields a hole concentration in the range $1–2 \times 10^{17}$ cm^{-3}.

The structural quality of epitaxial layers was characterized by high-resolution x-ray diffraction (HRXRD). Optical quality was evaluated by 300- and 4-K PL and measurement of minority carrier lifetime by time-resolved PL (TRPL). The samples were optically excited by a 0.98-μm diode laser, and the excess carrier concentration ranged approximately from 10^{16} to 10^{17} cm^{-3}. The PL emission was detected by an HgCdTe photodiode, as previously described [6]. The overall time resolution of the detection system is <5 ns.

Figures 2-2(a) and 2-2(b) show the HRXRD and PL results, respectively, of a typical AlGaAsSb/GaInAsSb/AlGaAsSb DH. The HRXRD curve exhibits a number of intense and sharp satellite peaks, which is indicative of high structural quality and compositionally abrupt interfaces. The more closely spaced thickness fringes associated with the 0.4-μm-thick GaInAsSb are easily resolved. The 4-K PL data shown in Figure 2-2(b) shows a full width at half-maximum (FWHM) of 9.2 meV. Similar structures that had undoped GaInAsSb layers had narrower FWHM of only ~5 meV. Furthermore, it was found that PL intensity was extremely sensitive to interruption time and ambient atmosphere when growth was interrupted after depositing the GaInAsSb layer [9], i.e., the upper GaInAsSb/AlGaAsSb interface. The highest PL efficiency was obtained only when the interruption period had a nominal partial pressure of TMSb $<1 \times 10^{-4}$ Torr and a growth interruption time <5 s. Since longer interruption times and higher TMSb partial pressure decreased PL efficiency, it is likely such growth-switching sequences introduce interface states where minority carriers recombine nonradiatively [9].
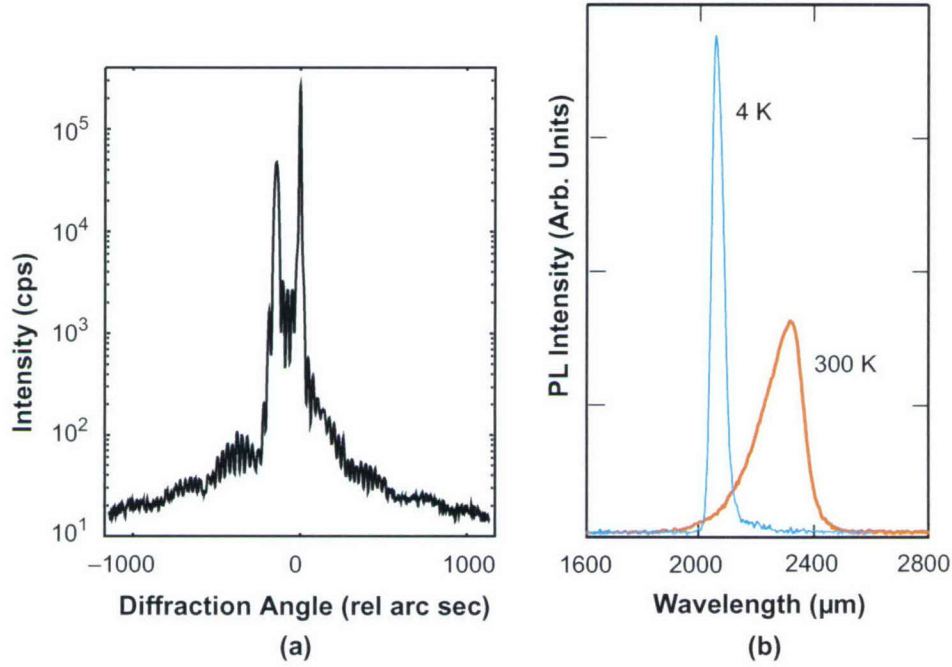
Figure 2-2. (a) High-resolution x-ray diffraction and (b) photoluminescence (PL) of AlGaAsSb/GaInAsSb/ AlGaAsSb double heterostructure.

Quantitative determination of interfacial quality was evaluated by analysis of minority carrier lifetime measurements to extract SRV [1],[6]. The lifetime is dependent on bulk and interfacial recombination processes and can be separated according to the equation

$$1/\tau_{PL} = 1/\tau_{BLK} + 2S/W \tag{2.1}$$

where τ_{PL} is the lifetime measured by PL decay, τ_{BLK} is the bulk lifetime, S is the SRV, which is assumed to be equal at the front and back heterointerfaces, and W is the active layer thickness. This approximation assumes that photon recycling effects [16] are negligible and that S is relatively small compared to the ratio of minority carrier diffusion constant D to W ($S < D/W$). These approximations are reasonable when W is less than 0.5 μm [17]. Thus, S can be determined from measurements of t_{PL} for samples with various thicknesses.

Minority carrier lifetime data measured by TRPL are shown in Figure 2-3 where $1/t_{PL}$ is plotted as a function of $1/W$. The data for the two sets of samples with different Al content demonstrate a linear dependence, and S is determined to be about 50 and 30 cm/s for Al content in AlGaAsSb of 0.2 and 0.25, respectively. These low values are significantly smaller than the value of 720 cm/s that was previously

9
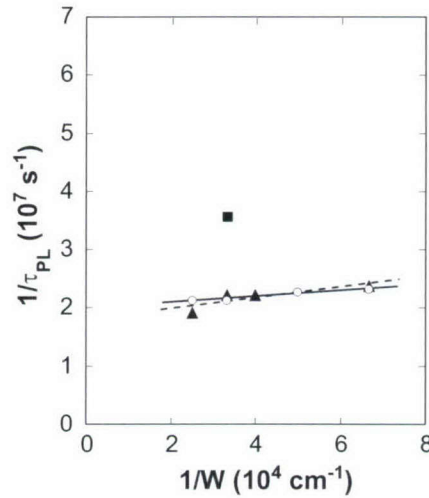
Figure 2-3. Inverse PL lifetime vs inverse GaInAsSb thickness of GaInAsSb/(Al)Ga(As)Sb double heterostructures: 0.2 Al content of AlGaAsSb (triangles); 0.25 Al content of AlGaAsSb (open circles); and GaSb capping layers (square).

reported for samples that were grown with interruption times on the order of minutes and similarly doped active layers [6]. That value of S did not account for photon recycling and was determined from samples with active layer thicknesses >1 μm. When photon recycling is factored into the estimation of S, it is only reduced by about 200 cm/s. Therefore, the benefits of minimizing growth interruption are apparent.

Also shown in Figure 2-3 for comparison is τ_{PL} for a DH sample with p-GaSb capping layers. This value of τ_{PL} is about 40% lower than that measured for the structure with similar thickness and AlGaAsSb capping layers. This reduction is likely related to a higher S value, although it cannot be determined from this single point. The lower lifetime for GaSb capped structures is consistent with previous observations [6] and is attributed to accumulation of electrons at the GaInAsSb/GaSb type-II interface and to thermionic emission resulting from lower electron confinement of GaSb confining layers [18]. It is likely that both the thin (2.5 nm) interfacial GaSb layers as well as long growth interruptions are responsible for the higher S values obtained for GaInAsSb/AlGaAsSb DHs in previous reports [6].

C. A. Wang   D. A. Shiau   D. R. Calawa
J. W. Chludzinski   D. Donetsky*   S. Anikeev*
G. Belenky*   S. Luryi*

*Author not at Lincoln Laboratory.

REFERENCES

1. R. K. Ahrenkiel, in *Minority Carriers in III-V Semiconductors: Physics and Applications,* Vol. 39 of *Semiconductors and Semimetals*, R. K. Ahrenkiel and M. S. Lundstrom, eds. (Boston, Academic, 1993), p. 39.

2. P. S. Dutta, H. L. Bhat, and V. Kumar, *J. Appl. Phys.* **81**, 5821 (1997).

3. T. J. Coutts, G. Guazzoni, and J. Luther, *Semicond. Sci. Technol.* **18**, S144 (2003).

4. C. A. Wang, H. K. Choi, S. L. Ransom, G. W. Charache, L. R. Danielson, and D. M. DePoy, *Appl. Phys. Lett.* **75**, 1305 (1999).

5. H. K. Choi, C. A. Wang, G. W. Turner, M. J. Manfra, D. L. Spears, G. W. Charache, L. R. Danielson, and D. M. DePoy, *Appl. Phys. Lett.* **71**, 3758 (1997).

6. D. Donetsky, S. Anikeev, G. Belenky, S. Luryi, C. A. Wang, and G. Nichols, *Appl. Phys. Lett.* **81**, 4769 (2002).

7. C. A. Wang, C. J. Vineis, H. K. Choi, M. K. Connors, R. K. Huang, L. R. Danielson, G. Nichols, G. W. Charache, D. Donetsky, S. Anikeev, and G. Belenky, *Fifth Conference on Thermophotovoltaic Generation of Electricity Proceedings* (American Institute of Physics, Melville, NY, 2003), p. 324.

8. O. J. Pitts, S. P. Watkins, C. X. Wang, V. Fink, and K. L Kavanagh, *J. Cryst. Growth* **254**, 28 (2003).

9. C. A. Wang, D. A. Shiau, M. K. Connors, L. R. Danielson, G. Nichols, D. Donetsky, S. Anikeev, and G. Belenky, *Symposium on Compound Semiconductor Photovoltaics Proceedings* (Materials Research Society, Warrendale, PA, 2003), p. 315.

10. B. R. Bennett, B. V. Shanabrook, and M. E. Twigg, *J. Appl. Phys.* **85**, 2157 (1999).

11. R. M. Biefeld, D. M. Follstaedt, S. R. Kurtz, and K. C. Baucom, *Seventh International Conference on Narrow Gap Semiconductors Proceedings* (Philadelphia, Institute of Physics Publishing, 1995), p. 13.

12. J. Wagner, J. Schmitz, D. Behr, J. D. Ralston, and P. Koidl, *Appl. Phys. Lett.* **65**, 1293 (1994).

13. C. A. Wang, H. K. Choi, and G. W. Charache, *IEE Proc.-Optoelectron.* **147**, 193 (2000).

14. C. A. Wang, H. K. Choi, D. C. Oakley, and G. W. Charache, *J. Cryst. Growth* **195**, 346 (1998).

15. C. A. Wang, *J. Cryst. Growth* **170**, 725 (1997).

16. P. Asbeck, *J. Appl. Phys.* **48**, 820 (1977).

17. S. Anikeev, D. Donetsky, G. Belenky, S. Luryi, C. A. Wang, J. M. Borrego, and G. Nichols, *Appl. Phys. Lett.* **83**, 3317 (2003).

18. D. Donetsky, S. Anikeev, G. Belenky, S. Luryi, C. A. Wang, D. A. Shiau, M. Dashiell, J. Beausang, and G. Nichols, *Sixth Conference on Thermophotovoltaic Generation of Electricity Proceedings*, (American Institute of Physics, Melville, NY, 2004).

3. SUBMICROMETER TECHNOLOGY

3.1 BUBBLES IN IMMERSION LITHOGRAPHPY

Immersion lithography [1] has recently reemerged and has quickly become a leading candidate for the extension of optical lithography to ever smaller dimensions. The current focus is on immersion at 193 nm. While many of the fundamental obstacles to immersion such as the availability of a suitable immersion fluid [2], gross resist performance under immersion [3], and hyper-numerical-aperture lens design [4] have been addressed, concerns still remain. Prominent in the list of remaining issues is the possibility for inhomogeneities in the immersion liquid to disrupt lithographic imaging.

As with conventional gas-ambient lithography, inhomogeneities can arise from gradients of temperature or pressure in the imaging medium, but new to immersion is the possibility of bubbles. Bubbles in the immersion liquid can arise from several sources. The liquid handling must be carefully designed to avoid injecting bubbles either through mixing with the ambient gas at the injection site or evolution of dissolved gas. In addition, bubbles can be entrained by the moving wafer at the three-phase liquid-wafer-ambient interface. Ridges in the resist can also trap bubbles as the liquid flows over them [5]. Networks of nanobubbles are known to form spontaneously at the interface between water and hydrophobic surfaces [6] although this problem can be avoided by degassing the water [7]. Finally, there is the possibility that evolution of gaseous photoreaction products from the exposed resist could create bubbles at the resist surface during or just after a laser pulse.

Numerical simulations can help us understand the impact of bubbles on immersion printing and, in particular, which types of bubbles will be the most problematic. The first simulation, shown in Figure 3-1,
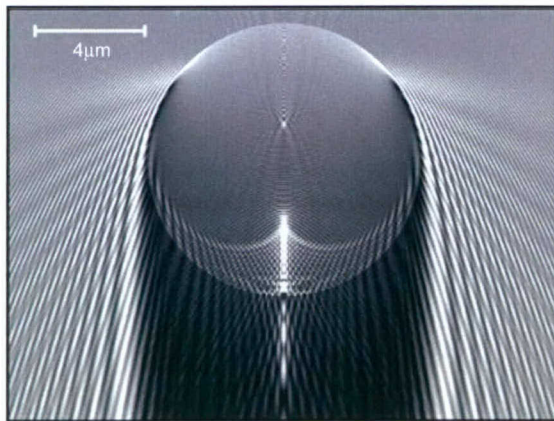
Figure 3-1. Light intensity distribution resulting from the interaction of an unpolarized 193-nm plane wave with a 10-μm gas bubble in water. The gray scale ranges from 0 intensity (black) to 2 times the incident intensity (white).

shows the intensity distribution of an unpolarized 193-nm plane wave incident on a 10-μm bubble in water. The electric field, and thus the intensity, was computed using the Mie series [8]; for the 10-μm bubble shown, 250 terms of the Mie series were used for good convergence. Scattering intensity does depend on polarization, but the differences between TE and TM are small for a 10-μm bubble.

The effect of a bubble on an image projected from a mask was simulated by a vector aerial image model [9] in which partial coherence is modeled by incoherently adding the aerial images arising from each point on the illuminator. In the presence of a bubble, each plane wave component from a point on the illuminator must be replaced by the corresponding set of waves computed by the Mie series as in Figure 3-1 above. Further complicating the simulation is the motion of the liquid, and thus the bubble, with respect to the wafer during the multipulse scanning exposure.

By using this combination of illuminator decomposition and Mie scattering, the aerial image of a periodic mask pattern in the presence of a stationary bubble was first calculated over an area covering the entire region of measurable shadowing by the bubble. For a 10-μm bubble 40 μm above the wafer surface, this region was about $\pm$80 μm horizontally from the bubble. The aerial image due to a moving bubble can then be obtained by considering the total distance $d = tv$ traveled by the bubble during the exposure interval, where t is the exposure time and v the bubble velocity with respect to the wafer. The most strongly affected feature is the one directly under the bubble halfway through the exposure. For this case the aerial images of individual periods of the otherwise periodic intensity pattern lying within $\pm d/2$ from the bubble can be extracted from the static aerial image and averaged to give the aerial image of this feature for the entire scanning exposure.

Two main factors affect the bubble impact: exposure time and bubble height above the wafer. A shorter exposure time enhances the impact of the bubble directly through a reduction in d, causing the feature to remain in the more heavily shadowed region for more of the exposure. The distance of the bubble from the wafer surface affects its lithographic impact in two ways. First, the shadows of different plane wave components of the aerial image are spread out over a larger area on the wafer, thereby reducing the impact on any one feature. In addition, bubbles farther from the wafer will move faster past the exposure region [10], increasing d and reducing the impact. Beyond several diameters from the resist surface, the impact of a single bubble diminishes, quickly becoming negligible. Both of these trends are seen in Figure 3-2, which shows aerial image simulation results for one period of a 100-nm 1:3 grating printed in the presence of a 10-μm bubble. The water velocity field was provided by Wei et al. [10] for the case of aligned flow under 200-Pa head pressure.

M. Switkes
M. Rothschild
M. S. Yeung*

Figure showing aerial image intensity plots.
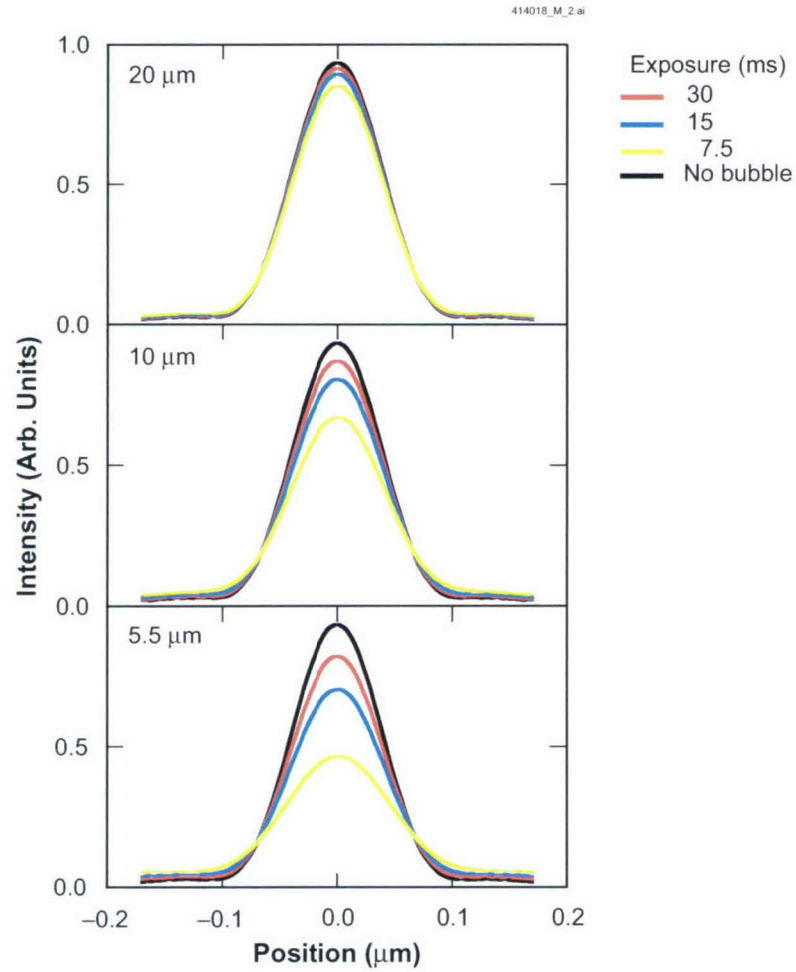
Figure 3-2. Aerial image intensity for a single 100-nm line in a 1:3 periodic grating printed in the presence of a 10-µm-diameter bubble. The distance of the bubble center above the resist, shown here for 5.5, 10, and 20 µm, as well as the exposure time strongly affect the impact of the bubble on the aerial image.

3.2   EFFECT OF SURFACTANTS ON LIQUID IMMERSION LITHOGRAPHY

Liquid immersion lithography has the potential to extend the 193-nm tool resolution to an estimated 60 nm or below [11],[12]. Liquids that will succeed as immersion fluids for this technique must provide fine resist lines that have smooth edges and straight profiles. Water is one of the most accessible and resist-friendly fluids we can use for liquid immersion lithography. It has a refractive index greater than air and is transparent at 193 nm. Therefore, it is an attractive candidate fluid for enhancing the resolution of 193-nm wavelength lithography. Some concern has been expressed, however, about the mechanical properties of water, including wetting, fluid flow, and the potential for formation of bubbles. The suggestion has been made that these properties could be improved with the addition of small amounts of surfactant to decrease the surface energy of the immersion fluid.

To evaluate the performance of surfactant solutions as immersion fluids, we exposed several resists through a contact phase mask, as shown in Figure 3-3, whose trenches were filled with various surfactant solutions. This allowed comparison of the imaging, through line edge roughness (LER) measurements between areas of the resist exposed while in contact with the immersion liquid (wet) and those in contact with the quartz mask (dry).

When a phase-contrast mask is irradiated, the light passes through two different media prior to reaching the resist. Because water and quartz have different refractive indices, the light waves moving through the different media become out of phase with one another. Destructive interference at the quartz/water edge results in a sharp reduction in light intensity, as seen in Figure 3-4. In these experiments this light intensity pattern exposes a positive photoresist, such that the resist areas exposed to high-intensity light undergo a chemical reaction and are removed by the developer. The areas exposed to
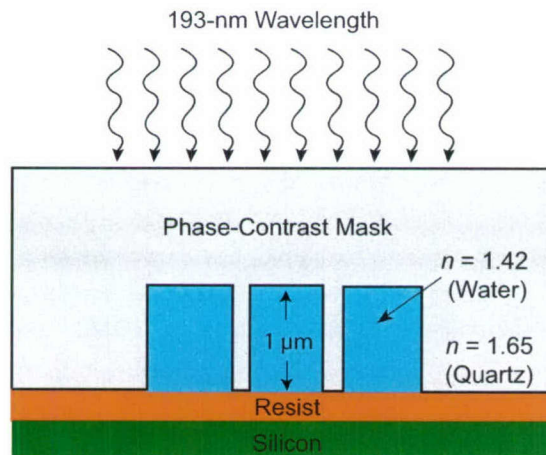
Figure 3-3. Direct imaging experiment using phase shift photomask. The quartz photomask is held in intimate contact with the resist-coated wafer. The channels in the mask are filled with an immersion fluid, water in this case.
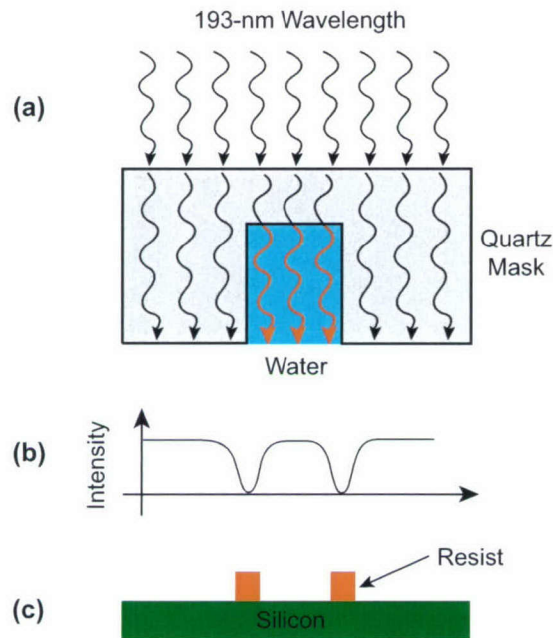
Figure 3-4. Schematic illustration of phase shift exposure process. (a) Quartz mask with water-filled channel. (b) Light intensity pattern. Intensity minima occur at the quartz/water edges because of destructive interference. (c) Pattern in positive photoresist after development. A resist line is patterned at each intensity minimum.

low-intensity light, at the quartz/water edges, are not removed and form the final pattern seen in Figure 3-4. Notice that each quartz/water edge in the mask forms a line in the photoresist. One edge of this resist line corresponds to the resist/quartz interface of the mask feature, and the other edge corresponds to the resist/wafer interface.

A chrome-coated quartz mask was etched to a depth of ~1 μm, and the chrome was then removed. This provided us with a phase-contrast mask to be used for hard contact exposure. The patterned area of the mask was flooded with immersion fluid. A resist-coated wafer was manually placed on the mask, bubbles and excess fluid were removed, and the mask and wafer were transferred to a jig for hard contact. The jig consisted of a 5×5 array of adjustable pins tightened and loosened across the wafer to equalize the contact pressure. With hard contact between the mask and wafer, water was trapped in the mask trenches. A green lamp was used to observe Newton rings during adjustment. Once best contact was achieved, the jig was placed in a fixed position on an isolation table beneath the laser exposure source.

The mask and wafer were then exposed to 193-nm light. Several dose matrices of spot exposures across the mask were initiated and controlled using a custom software program. The standard dose range was 10–40 mJ for the acid-catalyzed resist. Typical total exposure time ranged between 10 and 20 min.
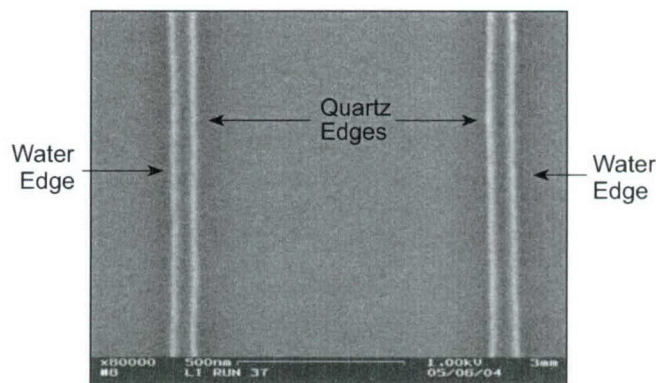
Figure 3-5. Top-down scanning electron micrograph of resist pattern showing two resist lines. For each line, one edge corresponds to the quartz side of the mask feature and the other edge to the water side.

After exposure, the wafers were baked at 115°C for 90 s and developed with a 0.26N tetramethyl ammonium hydroxide (TMAH) developer.

Wafers were observed using a field emission scanning electron microscope. For each wafer, best nominal dose was determined and imaged. A sample micrograph is shown in Figure 3-5. Ten successive images were taken along a pair of lines created by one raised feature on the mask. Three pairs of lines (at different locations) were photographed per wafer, and two wafers were exposed for each immersion fluid. In these experiments one resist was tested with three different immersion fluids: deionized (DI) water and two DI water solutions containing different surfactants. Two control samples, each using DI water without surfactant, were processed—one before and one after the test wafers were run. A software analysis program developed to determine LER values for each pair of lines was used to evaluate the effects of the various immersion solutions on the resist.

The rms roughness figures are nearly identical for each of the three fluids, indicating that the surfactants provide no advantage or disadvantage in regard to LER. Measurements of LER for each of the immersion fluids are seen in Figure 3-6. Note that some points for the AD07 surfactant fall far from the curve. These points occur on two of the edges of one spot.

The LER values of the quartz edges are compared to those of the liquid edges in Figure 3-7. Both edges provide the same roughness. Again, we have some measurements that are far off the curve. Note that these points occur on the quartz edges. A spot-by-spot review of the rms data suggested that the anomalies for both sets of data, which share the same location, are possibly due to physical damage of the mask features, i.e., chips in the quartz edges.

18
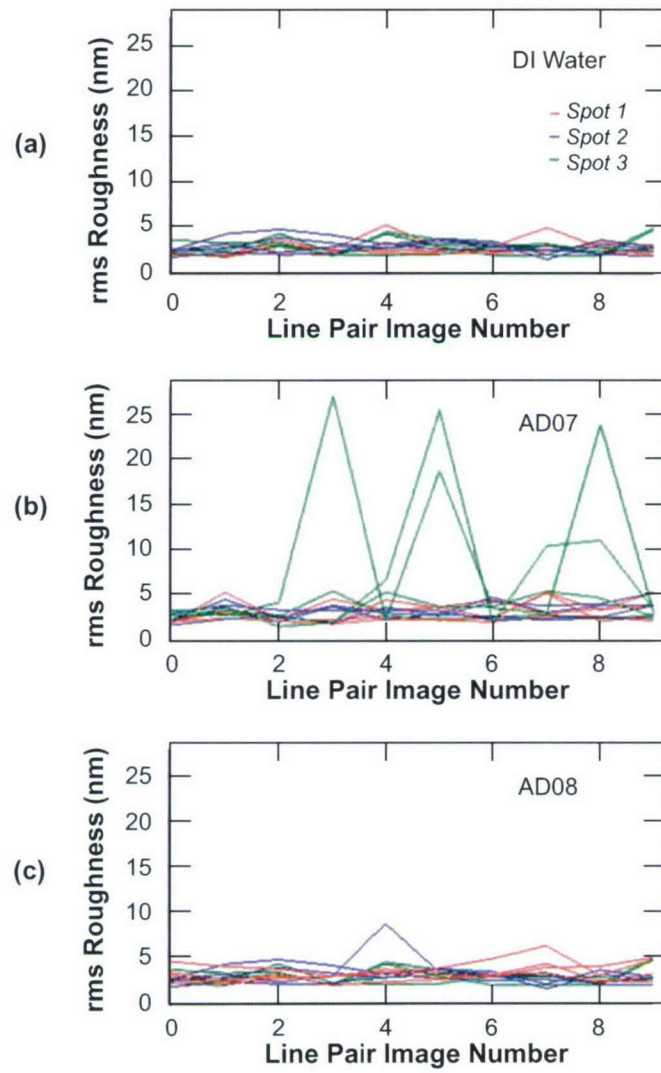
Figure 3-6. Measured line edge roughness (LER) for three immersion fluids: (a) deionized (DI) water, (b) DI water with AD07 surfactant, and (c) DI water with AD08 surfactant.
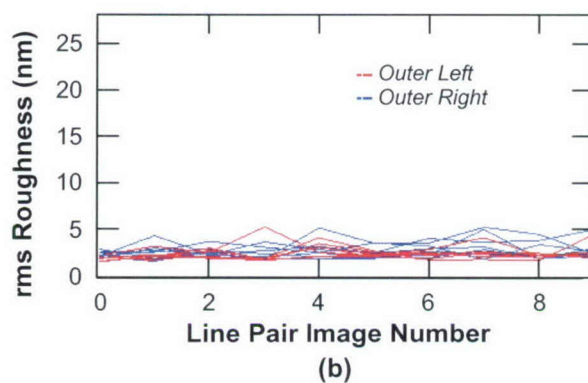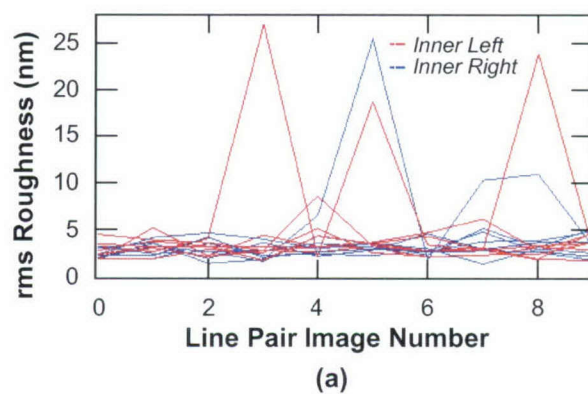
Figure 3-7. Comparison of LER for (a) inner left and right resist edges corresponding to the quartz side of the mask feature and (b) outer left and right resist edges corresponding to the liquid side of the mask feature.

The surfactants in the immersion fluids had no significant positive or negative effect on LER. Also, no difference was seen between the LER on the "water" and "quartz" resist edges. The control exposures done before and after the experiment showed similar rms results, indicating that the experimental conditions did not change during the experiment.

D. M. Lennon

REFERENCES

1. M. Rothschild, T. M. Bloomstein, R. R. Kunz, V. Liberman, M. Switkes, S. T. Palmacci, J. H. C. Sedlacek, D. Hardy, and A. Grenville, presented at the 48th International Conference on Electron, Ion, and Photon Beam Technology and Nanofabrication, San Diego, CA, 1–5 June 2004.

2. M. Switkes, M. Rothschild, R. R. Kunz, R. F. Sinta, P. M. Gallagher-Wetmore, V. J. Krukonis, and K. Williams, *Proc. SPIE* **5040**, 690 (2003).

3. A. K. Raub and S. R. J. Brueck, *Proc. SPIE* **5040**, 667 (2003).

4. W. Ulrich, H.-J. Rostalski, and R. Hudyma, *J. Microlith., Microfab., Microsyst.* **3**, 87 (2004).

5. A. C. Wei, M. El-Morsi, G. F. Nellis, and R. L. Engelstad, presented at the 48th International Conference on Electron, Ion, and Photon Beam Technology and Nanofabrication, San Diego, CA, 1–5 June 2004.

6. J. W. G. Tyrrell and P. Attard, *Phys. Rev. Lett.* **87**, 176104/1 (2001).

7. M. Switkes and J. W. Ruberti, *Appl. Phys. Lett.* **84**, 4759 (2004).

8. M. Born and E. Wolf, *Principles of Optics*, 3rd ed. (Pergamon, London, 1965).

9. M. S. Yeung, *Kodak Microelectronics Seminar Proceedings: Interface '85* (Eastman Kodak, Rochester, NY, 1986) p. 115.

10. A. C. Wei, G. F. Nellis, A. Y. Abdo, R. L. Engelstad, C.-F. Chen, M. Switkes, and M. Rothschild, *J. Microlith., Microfab., Microsyst.* **3**, 28 (2004).

11. *International Technology Roadmap for Semiconductors* (Semiconductor Industry Association, Austin, TX, 2003), pp. 1–18.

12. M. Switkes and M. Rothschild, *Proc. SPIE* **4691**, 459 (2002).

4. BIOSENSOR AND MOLECULAR TECHNOLOGIES

4.1 AFFINITY MAGNET CARTRIDGE DEVELOPMENT

The availability of rapid, portable polymerase chain reaction (PCR) machines for DNA analysis has generated the need for suitable sample preparation devices that can produce PCR-ready eluate from contaminated environmental and clinical samples containing PCR inhibitors. Current sample preparation protocols are primarily lab-bench techniques and often can handle only small quantities of sample per reaction. Our aim has been to develop a compact, fieldable, easy-to-use, self-contained cartridge that is able to concentrate target from larger samples as well as remove ubiquitous PCR inhibitors, for both liquid and solid sample types. The baseline laboratory procedure for this device is our Affinity Magnet (AM) protocol, which uses magnetic beads to concentrate target from a raw environmental or clinical sample to produce an eluate that is ready for PCR. We have now integrated the AM protocol into an AM cartridge that enables the user to process up to 5 mL of a liquid sample or 1 g of a solid that can be formed into a slurry, producing 0.5 mL of a PCR-ready eluate in 8 min or less.

The AM protocol has been reported previously [1]. Its goal is to concentrate targets of interest from liquids and semisolid slurries utilizing microscopic magnetic beads with non-antibody-based coatings that have affinities for the targets of interest. The beads are mixed with the sample containing the target to allow the target to adhere to the bead surfaces. A collection magnet is then used to remove the bead-target complex from the sample, thereby concentrating it. The target can then be processed in one of three ways—the bead-target complex can be directly subjected to PCR amplification, the target can be separated from the beads using specific elution buffers, or the DNA can be extracted from the target by subjecting the bead-target complex to the Simple Nucleic Acid Preparation (SNAP) protocol. The cartridge implementation of the AM protocol uses the second approach, in which the target is separated from the magnetic beads in an elution buffer, producing an eluate that is ready for PCR.

The magnetic beads consist of a magnetic core covered with a polymeric coating that is amenable to chemical functionalization. Tailored functional groups enable the selective capture of targets of interest, which may be DNA, vegetative bacterial cells, or spores. The coatings are not antibody based but are composed of simpler functional groups that are more robust than antibodies under the harsh conditions created with some types of environmental samples. We have developed and tested a large number of coatings using a range of functional groups, as well as elution buffers that enable effective separation of the target from the magnetic beads. The best-performing beads and buffers have been used in tests to evaluate the AM cartridge designs described here.

During the course of AM cartridge development, the design evolved over several generations, and many issues relating to the mechanics of fluid and bead manipulation were resolved during this rather complex evolution. Here, we report three versions of the AM cartridge, all capable of processing liquid and semisolid slurry samples. The first is composed of modified commercial off-the-shelf (COTS) parts and is

referred to as the two-valve COTS-based cartridge, the second uses a custom single-valve design, and the third is a single-valve cartridge that uses a COTS valve as the main element.

The basic two-valve COTS-based cartridge, shown in Figure 4-1, consists of three chambers separated by two valves. Each chamber is formed from a polypropylene or polystyrene tube cut to an appropriate length; the chambers are connected together with COTS polyacetal (Delrin) valves manufactured by John Guest International Ltd. All parts in the flow path of the sample are composed of FDA-approved materials that do not adhere to the target. The input (top) chamber serves initially as the sample collection chamber and subsequently as the waste chamber. It is a modified polystyrene test tube with a screw cap and contains magnetic beads with affinity coatings for the targets to be concentrated from the raw sample. It also contains a small Teflon ball to facilitate movement of liquid between the sample chamber and the processing chamber through the relatively small valve opening. The processing (middle) chamber is a modified polypropylene test tube and contains a collection magnet that collects and separates the magnetic beads from the raw sample. The eluate (bottom) chamber is a polypropylene screw-cap 1.5-mL vial, and it contains the elution buffer used to separate the target from the magnetic beads. The vial can be unscrewed from the cartridge body when processing is complete and sealed with the attached cap. The two valves are attached to a plastic backbone, providing rotational rigidity to the cartridge as well as stability when the cartridge is placed horizontally on a flat surface.

Figures 4-1(a) and 4-1(b) show the cartridge with two different styles of handles. The large handles in Figure 4-1(b) are injection-molded parts, originally designed for our LiNK (Lincoln Nucleic-acid Kit) 2.0 cartridge, which are attached to the input and output chambers to facilitate manipulation. The small handles in Figure 4-1(a), which are commercially available parts, are functionally identical to the handles in Figure 4-1(b); the larger handles were provided to make it easier to manipulate the cartridge while wearing heavy protective gear.

The cartridge is provided with all reagents and components necessary for sample processing. Magnetic beads are preloaded into the input chamber of the cartridge. The collection magnet is composed of neodymium-boron rare earth magnetic material and is nickel plated. It is retained in the processing chamber throughout sample processing. The eluate is deposited into a removable sample vial with an attached cap, enabling eluate storage for processing at a later date if desired.

The collection magnet contained in the processing chamber of the COTS-based cartridge is used to separate the magnetic beads and target from the sample. Requirements for this magnet are that it be strong enough to maximize magnetic bead collection in a minimum time, and small enough in volume to be submerged in the elution buffer to maximize target retrieval from the beads. We tested a number of configurations of this collection magnet, including a single magnetic sphere (diameter from 1/8 to 1/4 in.), a chain of multiple magnetic spheres, and a stack of magnetic cylinders. We also varied the location of the collection magnet during the target elution phase. Figure 4-2 shows the various configurations.

The single-sphere collection magnet required a collection time of at least 2 min to obtain adequate magnetic bead collection. The 10- and 15-ball chains provided good bead collection in 1 min; however, because of the small volume of elution buffer and the large elution chamber volume, all parts of the chain
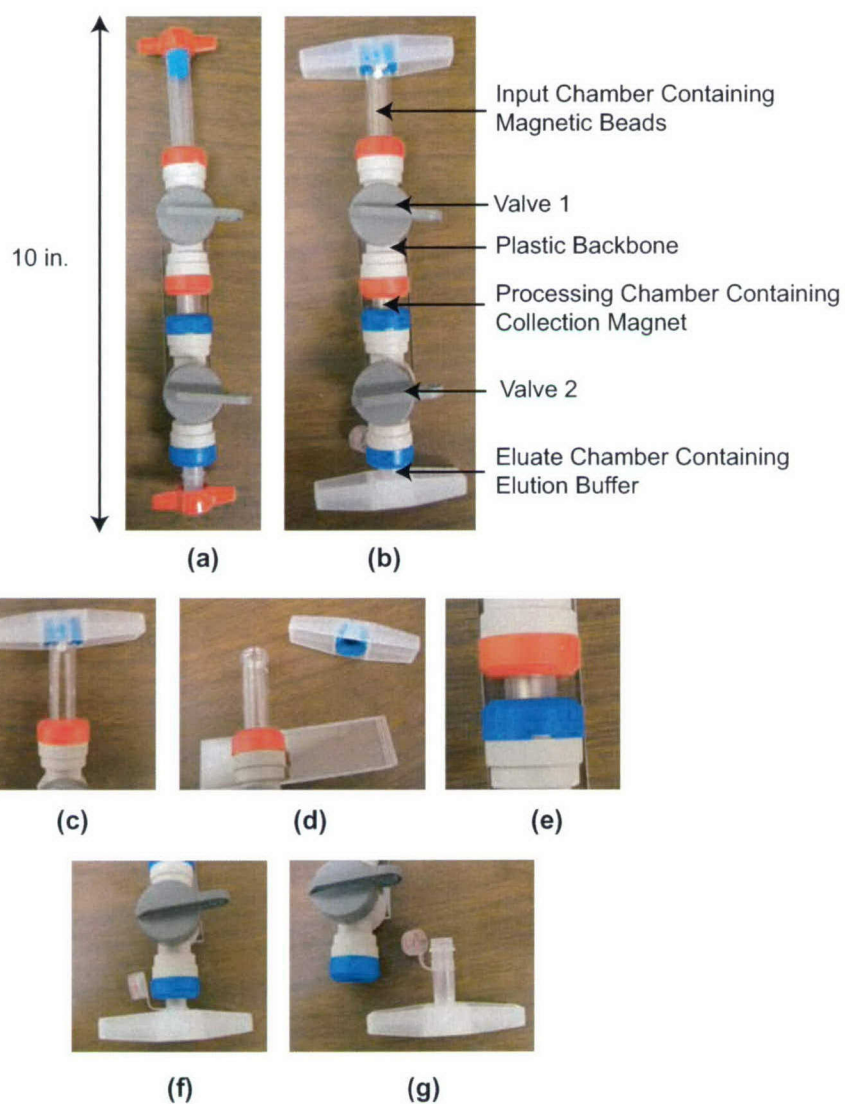
24

Figure 4-1. Two-valve commercial off-the-shelf (COTS) based Affinity Magnet (AM) cartridge: (a) Small-handle version; (b) large-handle version; (c) closeup of input chamber; (d) input chamber with cap removed; (e) closeup of processing chamber with collection magnet inside chamber; (f) closeup of eluate chamber; (g) eluate vial with attached cap, removed from cartridge.
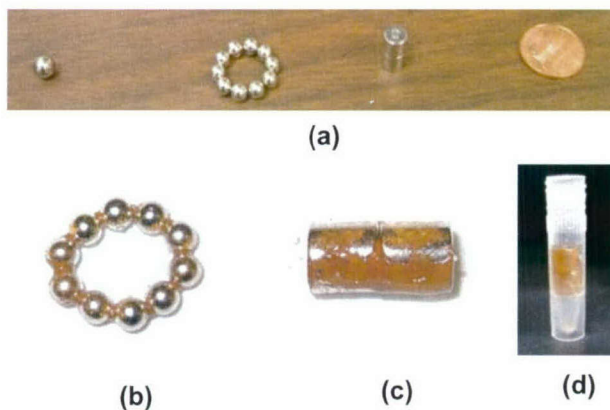
Figure 4-2. Variations on collection magnet: (a) Single sphere, 10-ball chain, two-cylinder stack; (b) closeup of 10-ball chain coated with magnetic beads, showing that most of the magnetic beads are in the crevices between the spheres; (c) closeup of two-cylinder stack coated with magnetic beads; (d) two-cylinder stack coated with magnetic beads, fully submerged in elution buffer in eluate chamber vial.

are not completely exposed to the buffer, making the elution step lossy. Additionally, the orientation of the magnetic field along the chain of spheres is such that the magnetic beads pile up primarily in the recesses between spheres. These areas are not exposed to the buffer as efficiently as the sides of the spheres, again making the target retrieval process lossy. For these reasons, we chose a two-cylinder-stack collection magnet. As shown in Figures 4-2(c) and 4-2(d), the majority of the magnetic beads are collected onto the sidewalls of the collection magnet, and the magnet is able to be completely submerged in the elution buffer.

The second version of the AM cartridge, shown in Figure 4-3, is a custom design, consisting of a single valve with a sample input chamber incorporated into the valve body and a removable eluate vial. The valve body with integrated sample input chamber is composed of polycarbonate, and the valve stem is formed from polyethylene. The eluate vial is a conventional 1.5-mL cryogenic storage vial. The valve stem has a small reservoir that accommodates the magnetic beads, which are captured into the reservoir by means of an external magnet that is part of the valve handle. Once the beads have been isolated from the raw sample, they are transferred to the eluate chamber containing elution buffer by turning the valve handle. The external magnet is removed from the valve allowing the magnetic beads to be immersed in the elution buffer. Once the target has been eluted from the beads, the external collection magnet is reinserted to collect the magnetic beads, leaving the elution buffer containing the target. An alternate design incorporates the collection magnet into the valve stem such that the magnet is not removable, which prevents possible accidental loss of the magnet. The advantages of the custom-designed cartridge over the COTS-based design are simplicity, ease of operation, compactness, and potentially lower per-unit cost. Our goal is to design the cartridge to be compatible with fabrication by injection molding.
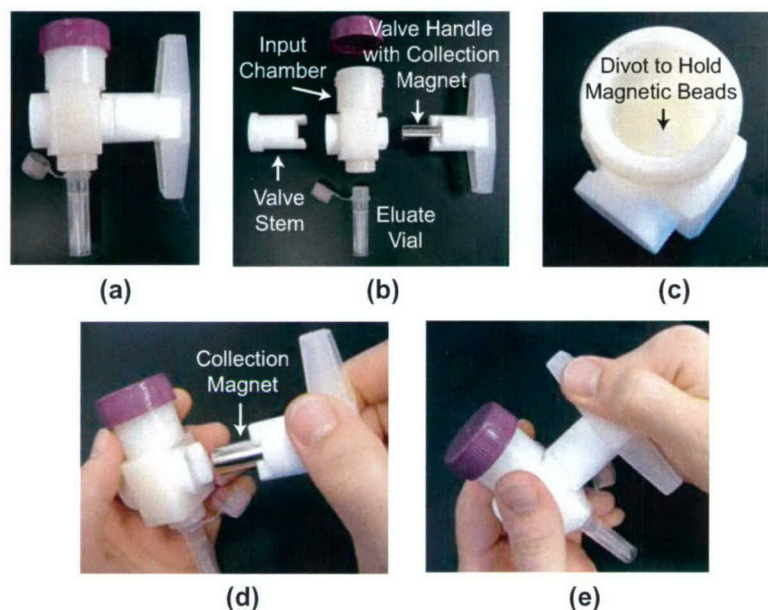
Figure 4-3. Custom-developed version of AM cartridge: (a) Assembled cartridge; (b) exploded view of cartridge; (c) closeup of divot in valve stem, to hold magnetic beads; (d) insertion of collection magnet; (e) turning of valve to transfer magnetic beads.
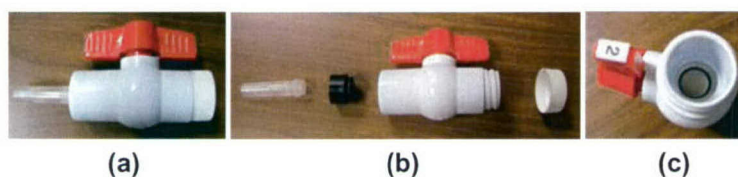
Figure 4-4. COTS-based AM cartridge: (a) Assembled view; (b) exploded view showing eluate vial, eluate vial plug, valve, and cap; (c) view of collection magnet inside plug in valve.

Figure 4-4 illustrates another custom single-valve version of the AM cartridge, based on a commercially available valve that has been modified to contain plugs to hold a standard 1.5-mL cryogenic storage vial and to form a chamber for the input sample. It also contains a thread that is compatible with a commercially available bottle cap. The collection magnet disc, again consisting of a rare earth magnetic material, sits inside a polypropylene plug (not shown) in the valve and is not removable. The cartridge is operated by loading the sample into the input chamber with the collection magnet not exposed to the chamber. After the beads are mixed with and allowed to capture the target, the valve is rotated 90° to expose the collection magnet to the input chamber. The beads collect onto the surface of the collection

magnet in less than 1 min, after which the valve is rotated 180° to expose the beads and target to the elution buffer for separation of the target from the beads.

Thus, three versions of the AM field-portable cartridge have been developed, in which all required reagents and components are contained within the cartridges, except for the water required to solubilize solid samples. We are continuing to test these cartridges on different matrices to determine extraction efficiencies.

L. Parameswaran
R. King
M. M. Angel

REFERENCE

1.   Solid State Research Report, Lincoln Laboratory, MIT, 2001:4, p. 19.

5. ADVANCED IMAGING TECHNOLOGY

5.1 FIRST TESTS OF THE ORTHOGONAL-TRANSFER ARRAY

In a previous report [1], we described a new sensor architecture for wide-field adaptive imaging in ground-based astronomy. This sensor consists of a two-dimensional array of independently controlled orthogonal-transfer charge-coupled devices (OTCCDs) that are used to perform electronic tip-tilt compensation. The addressing and control of each OTCCD is accomplished with on-chip switching logic in a manner similar to that of an active-pixel sensor (APS). Here, we describe additional design details of the control logic and initial tests on the first lot of these prototype orthogonal-transfer arrays (OTAs). The devices have been designed and fabricated for the Pan-STARRS (Panoramic Survey Telescope and Rapid Response System) program at the University of Hawaii under Air Force sponsorship.

To review the essential device features, we show in Figure 5-1 an OTA cell comprising an OTCCD, a logic control block, and associated control lines. Four versions of the OTCCD were included on the first design, two of them with 480×496, 12-μm pixels and the other two with 574×594, 10-μm pixels. In addition, two pixel designs were used for each pixel size. A complete OTA consists of an 8×8 array of these cells and occupies a die size of 49.5×49.5 mm. The OTCCD is read out via a three-phase serial register to a two-stage source-follower output amplifier. Each logic block is selected by row (R) and column (C) address lines, and three logic bits (D0–D2) then set the state of each addressed block. The logic circuitry in turn drives a set of pass transistors that serve as switches. One of its functions is to determine
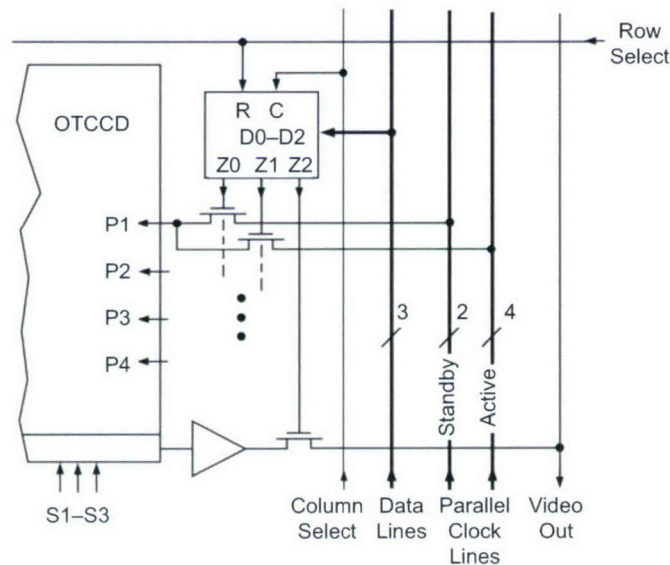

Figure 5-1. Schematic of orthogonal-transfer array (OTA) cell consisting of an orthogonal-transfer charge-coupled device, control logic, and the associated clock and control lines.

29
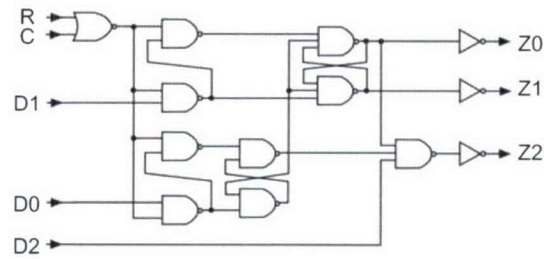
Figure 5-2. Schematic of the logic block adjacent to each OTA cell.
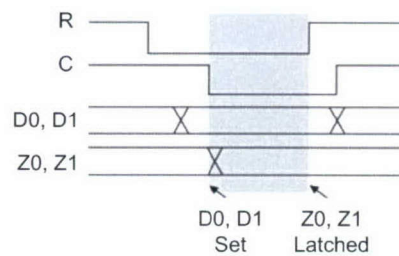
Figure 5-3. Logic timing for the latching of bits D0 and D1.

whether the four clocks of the OTCCD pixel array, P1–P4, are connected either to a set of clock waveforms common to all cells, to dc standby levels, or left floating. The other function is to switch the output video signal from each cell to a column video bus that is shared by all the cells in a column.

Figure 5-2 is a schematic of the logic located next to each OTCCD, and Figure 5-3 depicts the logic timing. Simultaneous low voltages on the row and column select lines enable the cell to respond to the data bits, and two of these bits (D0, D1) are latched when one or both select lines return to the high state. The D2 bit, which determines the state of the video-output pass transistor, is not latched because the intended operating modes of the device for video readout did not require it. This enabled us to simplify the logic somewhat. The logic is made in nMOS, and all gates, except the final inverters that provide the output levels Z0–Z2, are powered with +5 V and can be driven with 5-V CMOS-compatible logic levels. The final output inverters must provide a higher voltage to drive the pass transistors because the clock and video voltages to be switched are higher than 5 V. The drain supply of these circuits can be as high as +15 V. Table 5-1 describes the relationship between the input and output data levels and their effects on the parallel-clock and video-output control.

One significant feature of this device is the metallization process employed. Because of the extensive crisscross network of metal clocking and control lines, a two-level metal process was necessary. We used a fully planarized dry-etch damascene process with tungsten plugs and Ti/TiN/AlSi metallization, in contrast to our prior CCD processes, which used borophosphosilicate glass (BPSG) reflow and

30

wet-etched contacts and metal (AlSi). Compared with wet etching, the dry etching enabled finer geometries in both contact sizes and linewidths, features that are important in minimizing dead space between the cells. It also allows thicker interlevel dielectric layers without expanding contact sizes (the dry contact etch is highly anisotropic), and this should improve yield against interlevel shorts and reduce capacitive loading. The initial device yields from this new process appear to be at least as good as the prior
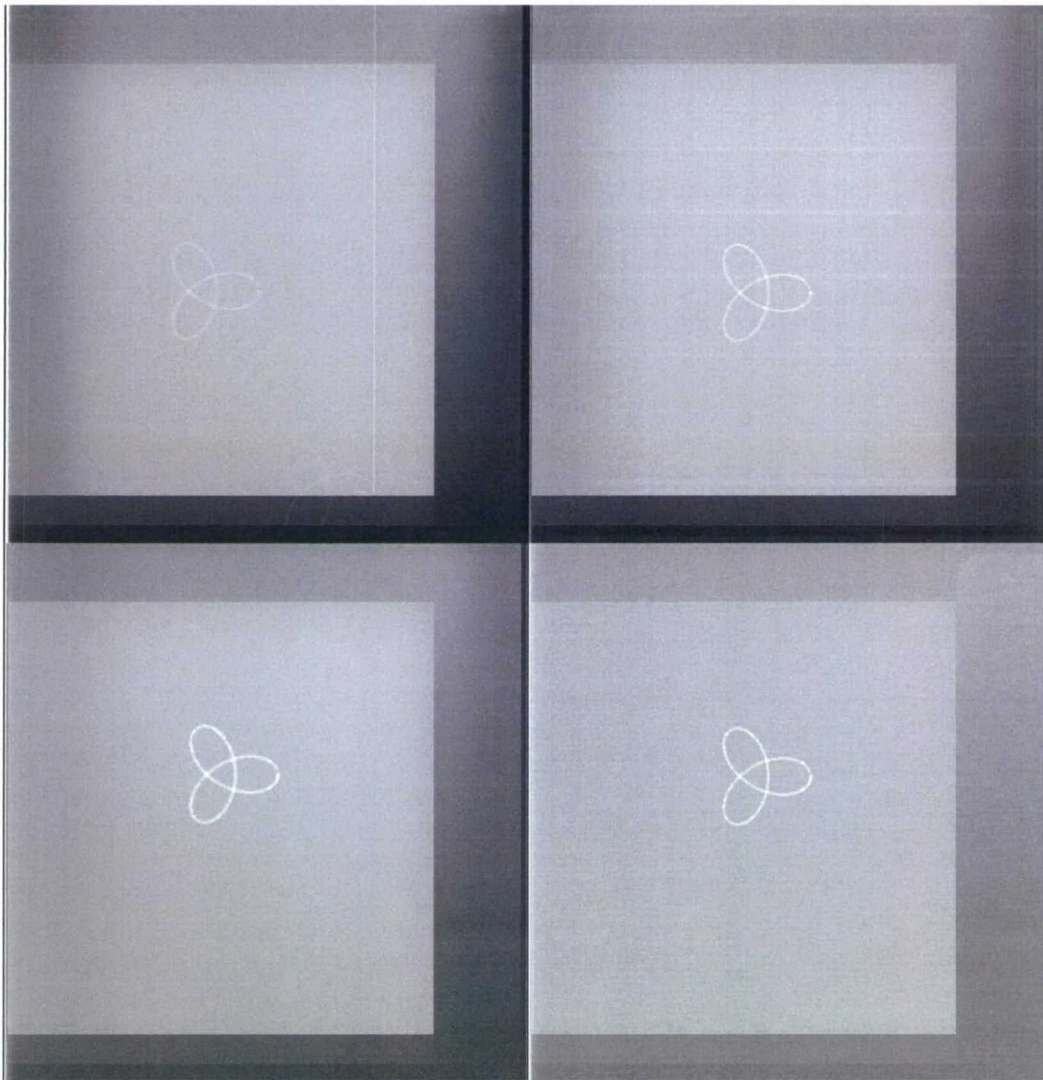

Figure 5-4. Composite image from the four cells of a 2×2 mini-OTA (MOTA) using a fixed light spot focused onto each cell with the CCD clocks programmed to shift the charge in a simple pattern of loops.

TABLE 5-1

Relation Between the Input Bits (D0–D2) and the Output Bits (Z0–Z2), Parallel Clock (P1–P4) States, and Output Video

D0	D1	D2	Z0	Z1	Z2	P1–P4	Video
0	0	0	0	1	0	Active	Off
0	0	1	0	1	1	Active	On
0	1	X	1	0	0	Standby	Off
1	X	X	0	0	0	Floating	Off

CCD processes, though further evaluation remains to be done. In particular, the more subtle effects of dry-etching steps, such as radiation damage that can raise device noise, need to be studied.

The first lot contains a variety of OTAs having both 2×2 and 8×8 arrays of OTCCD cells. We chose to focus on the 2×2 arrays, which are termed mini-OTAs (MOTAs), for initial system setup. Figure 5-4 is a sample image from the four cells of a MOTA under test at a wafer probe station at room temperature. The MOTA in this case had 12-μm pixels with the pixel design described in [2]. These images were generated by focusing a light spot through the microscope eyepiece onto the device. Each MOTA cell was addressed for active clocking of the pixel gates, and the gates were clocked to shift the charge in x and y to create the image. The background dark current shows bands of reduced signal level along the sides of each cell image. To prevent pileup of charge at the cell boundaries, we placed charge overflow drains along the top and sides of the pixel array. These drains sink the charge that is clocked past the cell boundaries on three sides, while the serial register collects charge when the array is clocked downward. The darker bands in these images are the rows and columns that lost dark current during shifts into these charge sinks.

B. E. Burke
M. Cooper
D. Young

REFERENCES

1. Solid State Research Report, Lincoln Laboratory, MIT, 2004:3, p. 23.

2. B. E. Burke, R. K. Reich, E. D. Savoye, and J. Tonry, *IEEE Trans. Electron Devices* **41**, 2482 (1994).

6. ANALOG DEVICE TECHNOLOGY

6.1 ULTRALINEAR, MULTIGIGAHERTZ CHIRP GENERATOR USING DIGITAL COMPENSATION

Linear chirp generation using a swept local oscillator (SLO) is a key functional element of wideband analog rf signal processing systems. In compressive receivers [1], for example, an input signal is first mixed with a linear chirp and then fed into a dispersive delay line to perform spectral analysis. High SLO linearity (frequency vs time) is required to support wide dynamic range. Here, we report the demonstration of a highly linear SLO that operates from 15.5 to 24 GHz over a chirp length of 60 ns.

Previous work has demonstrated the advantages of using predistortion, or compensation, to linearize a microwave voltage-controlled oscillator (VCO) for compressive receiver SLO applications by using polynomial fitting to a static VCO tuning characteristic and applying the predistortion in a fixed analog fashion [2]. Although acceptable linearity was reported over SLO chirp slopes up to 1.0 MHz/ns (1 GHz over 1 μs), this technique has two primary limitations. First, the number of polynomial coefficients is limited because of the increased complexity of both the circuits and calibration with higher orders. Second, the polynomial coefficients are set with potentiometers and must be hand adjusted for good performance. Increased performance beyond the capabilities of traditional SLO techniques is desired for compressive receiver applications with 150 times steeper chirp slopes and 10 times faster repetition times. The proposed digital compensation technique addresses these challenges, and the digital nature of the compensation enables automated real-time calibration of variations due to temperature or aging.

As shown in Figure 6-1, an SLO can be realized by applying a voltage ramp to a VCO. For a VCO with a nonlinear tuning characteristic defined as $F_{VCO}(V_C)$, and assuming ideal dynamics, a perfectly linear frequency chirp is achieved when the voltage V_C matches the inverse of the tuning characteristic F_{VCO}^{-1}. The task of compensating the system to achieve minimum linearity error ΔL is to generate a voltage ramp that best approximates the ideal inverse curve, designated $V_{Co}(t)$.

To implement a digital compensation, $V_{Co}(t)$ must be divided into N discrete segments. A first approach might be to perform a sample and hold on $V_{Co}(t)$, but one quickly concludes that the step function provides a poor ramp approximation. A second approach might be to start with a nominal ramp slope and then add a compensation term at each segment to account for the frequency offset. Although this is a better approximation, the resulting ramp is not monotonic and leaves a moderate sawtooth residual.

A cleaner approach is to perform a first-order hold of the $V_{Co}(t)$, which creates a piecewise linear segmentation. In this way, the slope of V_C can be adjusted multiple times during the chirp, and the integrity of the overall ramp waveform is maintained with continuous first and second derivatives. Although the circuit implementation of the first-order sample and hold is slightly more complex, this is more than overcome by a relaxed burden on the digital-to-analog converter (DAC). As shown in Figure 6-2, N can be
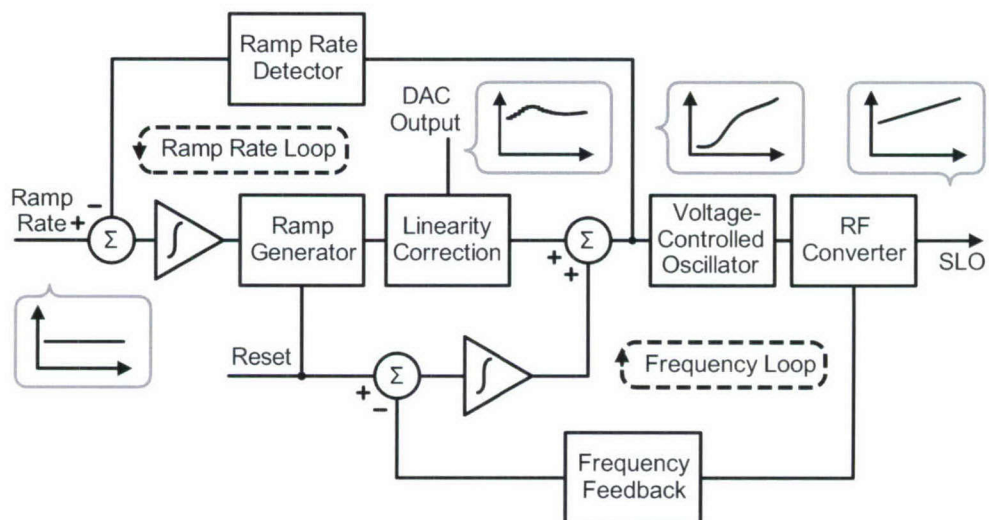
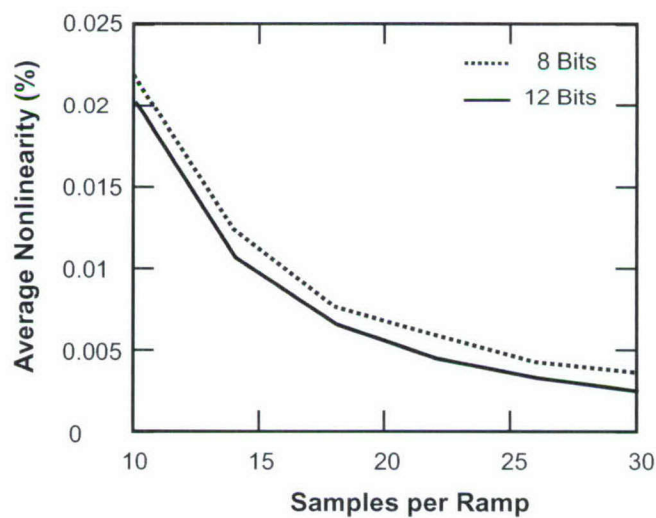*Figure 6-1. Block diagram of digitally compensated swept local oscillator (SLO).*

Figure 6-2. Simulated average nonlinearity vs digital-to-analog converter (DAC) speed and resolution.
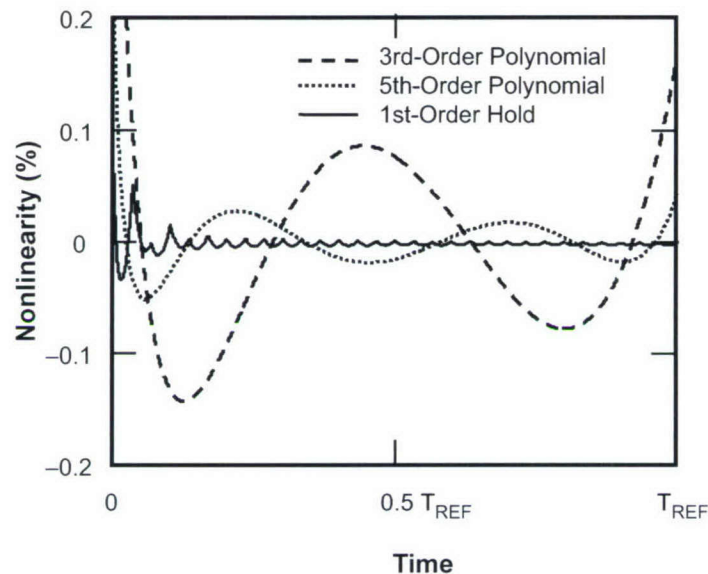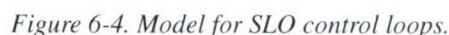
Figure 6-3. Simulated comparison of polynomial compensation techniques with the proposed digital compensation. The uncompensated nonlinearity is 4%, or equivalent to a voltage-controlled oscillator (VCO) sensitivity ratio (SR) of 2.9.

as small as 10–15 with only 8 bits of DAC resolution, and still the compensation maintains very good linearity improvements.

A mathematical comparison of the proposed first-order hold scheme is made with the more traditional polynomial data fits, as seen in Figure 6-3. Notice that while the polynomial errors are sizable across the entire ramp, the first-order digital compensation quickly converges to near-zero error levels for all points during the ramp, except for the areas with the most severe slope variations.

The control block diagram for the SLO is shown in Figure 6-4. To maintain a high degree of precision in the output frequency chirp, two control loops are required to correct for frequency offset and ramp slope. Although the two control loops operate on the same voltage waveform, they can each be analyzed independently because of the serial connection. A closed-loop bandwidth of approximately 5 kHz is used for the phase-locked loop (PLL), and 15 kHz is used for the ramp rate loop. Lower bandwidths are chosen for these loops to limit overcorrection of error terms.

The sawtooth shape of the control voltage is created by integrating a constant corresponding to the ramp rate and then resetting the integrator output for each new chirp. A convenient realization of this function with circuit elements is a constant current source fed into a capacitor and shunt by a reset switch.

Figure 6-4. Model for SLO control loops.

With low switch R_{ON}, the reset time can be very fast, and more important, the output can be set to a known potential at the beginning of each new ramp profile.

To realize the scaling of the compensation with the ramp rate feedback term, a multiplication and addition is performed with a high-bandwidth four-quadrant voltage multiplier. The multiplier output voltage subsequently is converted into a reference current and then mirrored for the ramp integration. A zero is added to the cascode current mirror to improve bandwidth, which is measured at >300 MHz. To realize the ramp scaling and offset, high-voltage output amplifiers with very high slew rate and small signal bandwidth are used.

A system clock of 375 MHz is used to clock the DAC and field-programmable gate array (FPGA). The FPGA is designed to provide digital control for the entire board, including the DAC as well as the ramp reset signals and off-board serial communication. Although the logic values for the reset are provided by the FPGA, the actual reset pulse is retimed with a master clock to achieve low jitter.

An ideal VCO for the linear upchirp would have very high tuning bandwidth and linearity, and output frequency range matching the application requirements. However, at microwave frequencies the availability of such components is limited, and therefore a VCO with acceptable linearity (sensitivity ratio <3), high tuning bandwidth (>200 MHz), and wide tuning range (12–18 GHz) is selected. As a result, F_{VCO} must be upconverted and then doubled to result in F_{SLO}. The block diagram for these operations is shown in Figure 6-5 and consists of connectorized commercially available rf components. Although not shown, filters and isolators are used to minimize the effect of harmonic spurs and reflections. The feedback for the PLL is taken with a coupler before doubling because of frequency limitations in available prescalers.

There is currently no practical way to measure frequency directly at the SLO output of 15.5–24 GHz with high chirp rates of 140 MHz/ns. Therefore, an indirect approach is used based on high-speed sampling of the $F_{SLO}/16$. The signal to be measured is coupled from the PLL feedback and fed into a high-speed digital sampling oscilloscope. Data from multiple chirps is acquired and saved by the oscilloscope and then
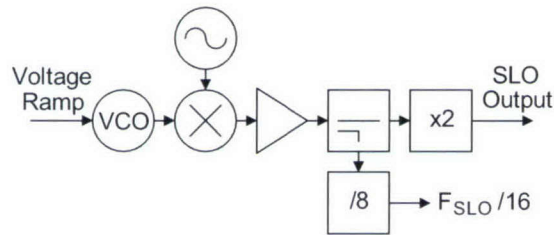
36

Figure 6-5. RF module block diagram including VCO. For clarity, the filters, isolators, and attenuators are not shown.

subsequently post-processed by a separate computer. Although an increased number of chirps is desirable to reduce sampling noise, in practice the maximum data set is set to about 100 ramps to achieve reasonable processing time.

The first step in extracting the SLO linearity vs time is to determine the positive zero-crossings of the sampled $F_{SLO}/16$. Linear interpolations of the zero-crossings are made for accuracy, resulting in an asynchronous sampling of time and F_{SLO}. The multiple chirps are then divided into single chirps by triggering off the ramp reset, which is easily distinguishable. To average the multiple data sets together, each set of asynchronous data is interpolated into a synchronized set of oversampled data. The averaged data from all ramps is then fit using a least-squares algorithm.

A graphical user interface was created to optimize and then automate the selection of compensation data. Because of a fixed time offset between the reset action used to calculate the linearity and the location of each compensation data point, it is not difficult to locate the appropriate compensation time slot (index) that needs to be adjusted.

The effect of changing the value at a single index is seen not just at the corresponding offset in the chirp but rather by the entire ramp. To understand this empirically, consider a constant compensation W_{DAC} that creates a linear voltage ramp V_C and results in linearity error ΔL, as shown in Figure 6-6(a). In Figure 6-6(b), an incorrect response to correct for this error is shown, in that the ramp rate is adjusted proportionally to the linearity error. The correct compensation is shown in Figure 6-6(c). In this case the derivative of the error from Figure 6-6(a) is subtracted from the compensation. Notice that the ramp rate feedback loop will provide the correct overall slope, and the compensation values only supply relative weighting. Therefore, a single index value should not be changed independently, but rather the entire data set should be calculated as a whole.

A data set of measured results from a 15.5–24-GHz SLO is shown in Figure 6-7. The peak nonlinearity is approximately 0.4%, with rms error <0.1%. Notice that the dominant nonlinearity is at very high bandwidth compared with expected performance. Because of the limited bandwidth of both the ramp generator board and the VCO itself, these high-frequency errors are likely due to dynamic effects of a very
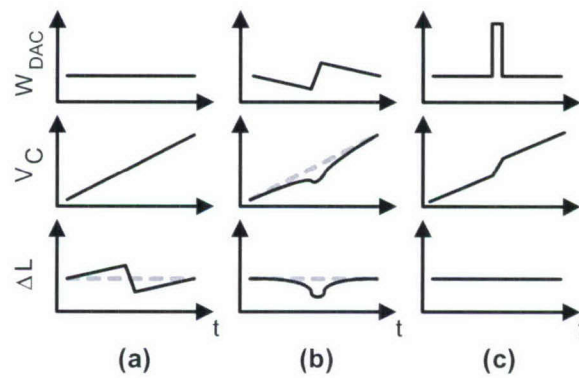
Figure 6-6. Illustration of compensation adjustments and the effect on linearity (a) with effectively no compensation, (b) showing an incorrect attempt to resolve the error from (a), and (c) with the correct compensation that results in a linear output.
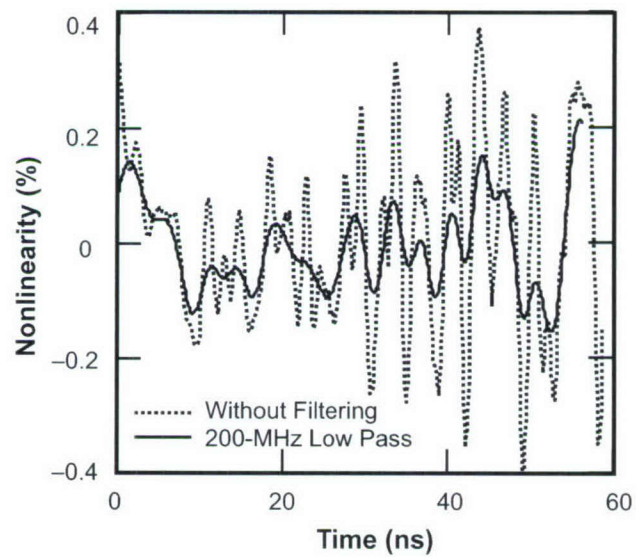

Figure 6-7. Measured nonlinearity data using digital compensation technique. The solid line shown has been passed through a 150-MHz digital low-pass filter, which corresponds to the maximum frequency response of the compensation.

steep chirp slope. Group delay variations with frequency and reflections can effectively modulate the SLO with an error term that increases with chirp slope. The digital compensation has reduced the steady state VCO nonlinearity errors by over an order of magnitude.

In summary, a digital compensation technique for a VCO-based SLO has been presented. The proposed circuit applies the correction factor to the ramp rate term within a feedback loop to achieve a smooth and linear upchirp. The proposed method is used for generating an ultralinear, multigigahertz SLO with very high chirp rate. Run-time linearity measurement and autocalibration techniques are presented. Measurements demonstrate a linearity error less than 0.4% across 15.5–24 GHz with a chirp length of 60 ns. The VCO nonlinearity contribution is reduced to the level of or below dynamic errors such as nonlinear group delay and measurement accuracy. These data suggest that the technique is well suited for generating SLOs for demanding applications such as high-performance compressive receivers and radar measurement systems.

M. Z. Straayer
A. V. Messier
W. G. Lyons

REFERENCES

1. W. G. Lyons, D. R. Arsenault, A. C. Anderson, T. C. L. G. Sollner, P. G. Murphy, M. M. Seaver, R. R. Boisvert, R. L. Slattery, and R. W. Ralston, *IEEE Trans. Microw. Theory Tech.* **44**, 1258 (1996).

2. P. J. Burke, *MTT-S International Microwave Symposium Digest* (IEEE, Piscataway, NJ, 1994), Vol. 2, p. 957.

7. ADVANCED SILICON TECHNOLOGY

7.1 INVESTIGATION OF WAFER-TO-WAFER ALIGNMENT TOLERANCES FOR THREE-DIMENSIONAL INTEGRATED CIRCUIT FABRICATION

We have previously demonstrated three-dimensional circuit integration techniques based on silicon-on-insulator (SOI) substrates using adhesive bonding [1] and oxide bonding [2] to attach the active circuit layers (referred to as "tiers"). In both cases the buried oxide acts as an etch stop during removal of the handle substrate. After the removal step inter-tier vias are formed to electrically connect the circuit layers.

For optimal circuit density the minimum pitch of inter-tier vias should be comparable to that of intra-tier vias for the particular fabrication technology being used. The pitch is determined by the via size, which is dependent upon the achievable aspect ratio, and by the wafer-to-wafer alignment tolerance, which is primarily constrained by the alignment system being used. To the present we have been using a modified mask aligner that gives us a tolerance of ± 2 μm. This relatively large value can impose constraints on the application of three-dimensional integration to some circuit designs. To improve upon this figure, some of the techniques used in wafer steppers may be applied to the problem of accurate wafer-to-wafer alignment. It is evident, however, that die placement distortions that arise from various processes may limit the achievable pitch as the alignment accuracy approaches zero.

Here, we report results of an analysis of alignment data obtained from wafers aligned and oxide bonded in our facility. Also presented is a description of an advanced wafer alignment tool currently under development. Two types of wafer pairs were measured for this work. Wafers from the first type, referred to as metal-only pairs, were fabricated by patterning a 630-nm-thick Ti/AlSi/Ti/TiN metal layer that was deposited on thermally grown SiO_2 on bulk silicon substrates. The metal layer was then covered with plasma-enhanced tetraethylorthosilicate (PETEOS) and low-temperature oxide (LTO) films and polished by chemical-mechanical planarization. No other lithographic layers were defined on these wafers. The other type, referred to as device pairs, consisted of single-metal photodiode wafers fabricated in bulk silicon and three-metal CMOS wafers fabricated using a 180-nm fully depleted SOI (FDSOI) process. All lithographic layers on all of the wafers were defined using a Canon FPA-3000 EX4 wafer stepper and a die-to-die spacing of 22 mm.

The wafers were aligned to each other using a modified Karl Süss MA-6 wafer aligner with infrared optics. The details of the oxide bonding and handle removal processes have been described elsewhere [2]. In the case of the metal-only pairs, the top tier was exposed by stopping the silicon etch on the thermal oxide; for the device pairs, the buried oxide layer on the CMOS tier served as the etch stop. Once the silicon was removed, overlay marks that had been fabricated in the alignment metal layers were measured using an OSI Metra 2100, which has a measurement accuracy of ~15 nm and is repeatable to ~5 nm.

A total of 26 metal-only pairs and 9 device pairs were measured. In some cases bonding voids were present and the overlay data for missing die could not be obtained. One measurement site at each die center

was used to obtain grid error data. No intra-die measurements were made. A total of 376 die from the metal-only pairs and 158 die from the device pairs were analyzed.

The overlay tool calculates grid correction values from the formulas [3]

$$X_{error} = X_{trans} - R^*Y_{pos} + X_{scale}^*X_{pos} - O^*Y_{pos} + X_{res}$$

$$Y_{error} = Y_{trans} - R^*X_{pos} + Y_{scale}^*Y_{pos} + Y_{res}$$

where $(X,Y)_{error}$ are the measured errors at each site in μm, $(X,Y)_{pos}$ are the site positions in μm, $(X,Y)_{trans}$ are the translation offsets in μm, R is the rotation in ppm, $(X,Y)_{scale}$ are the scale (or expansion) terms in ppm, O is the grid orthogonality (or the difference in rotation between the two axes) in ppm, and $(X,Y)_{res}$ are residual errors in μm. The translation offsets are calculated by finding the mean of all the site errors. Least-squares regression (LSR) is used to fit the data to determine the values for rotation, orthogonality, and scale. Residual errors from the LSR fits represent nonlinear and random effects and are reported as the rms for both axes. These grid correction values are normally used to correct for stepper errors during process development. For wafer-to-wafer alignment, however, the differences in rotation and scale between the two axes cannot be compensated; thus, average rotation and scale values were calculated and applied to each measurement.

Histograms of the die offsets with corrections applied for translation and rotation are plotted in Figures 7-1(a) and 7-1(b) for metal-only and device pairs, respectively. This represents the alignment error that would be possible in an ideal aligner without substrate temperature control to correct for scaling effects. The mean 1σ values are approximately 0.3 μm for the metal-only pairs and 0.4 μm for the device pairs. These values are in good agreement with those reported for wafers aligned in a commercially available aligner [4] and for a system constructed at the University of Tokyo [5]. When scaling errors are
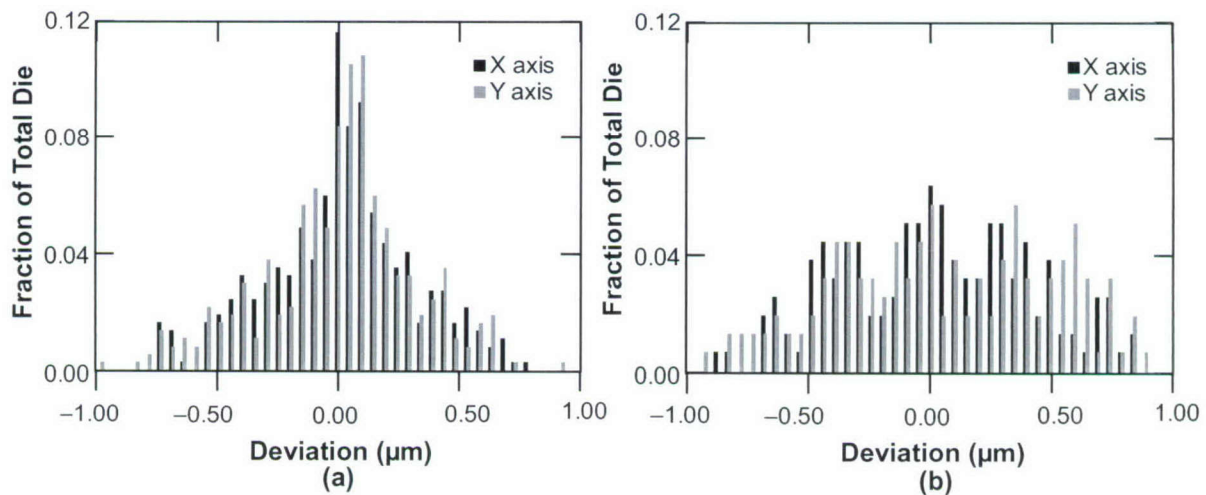

Figure 7-1. Alignment error distributions corrected for translation and rotation for (a) metal-only pairs and (b) device pairs.
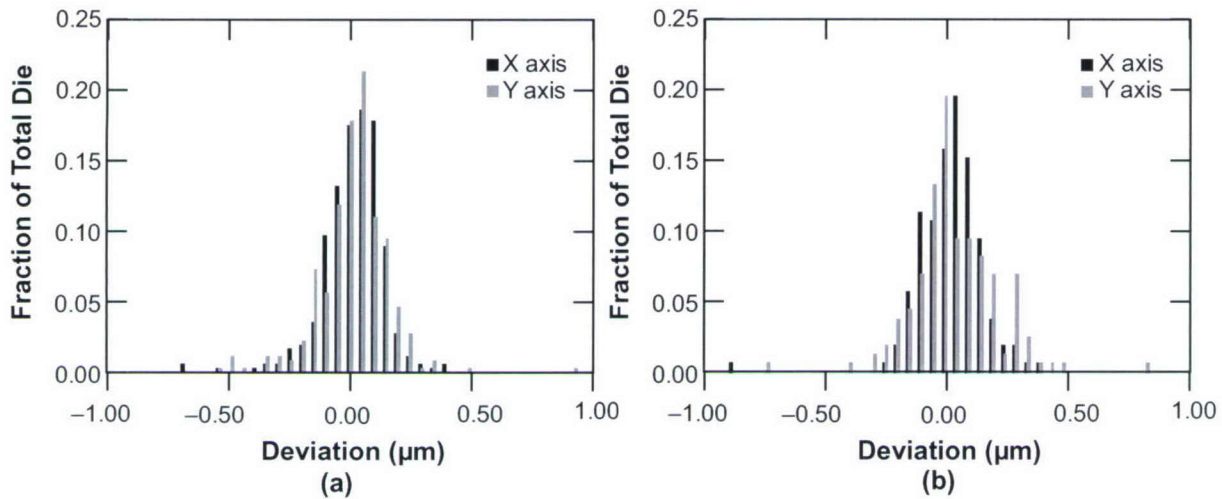
42

Figure 7-2. Alignment error distributions corrected for translation, rotation, and scale for (a) metal-only pairs and (b) device pairs.

removed from the data, the 1σ values reduce to ~0.13 μm and ~0.16 μm for the metal-only and device pairs, shown in Figures 7-2(a) and 7-2(b), respectively. The data are summarized in Table 7-1.

We have undertaken the design and fabrication of an alignment tool based on criteria determined from this data. A precision *XY* air-bearing stage controlled by an environmentally compensated laser interferometer is used to map the wafers to measure scale and to select best matches between wafers. To compensate for differences in scale, the substrates can be heated. The data indicate that the scale has a range of ±20 ppm, which corresponds to a temperature range of about ±8°C for silicon. The absolute alignment accuracy is dictated by the mechanics of the system and the position-sensing method being used. Infrared imaging using two InGaAs cameras with subpixel edge detection provides a relative line position resolution of ~50 nm. The cameras are spaced 44 mm from the center to provide a rotational resolution of ~1 μrad. A six-axis piezoelectric stage with nanometer-scale resolution provides *X, Y, Z,* Θ, tilt, and tip motions for the bottom wafer while the top wafer remains fixed. From these design considerations an alignment accuracy of ±125 nm is a reasonable "best-case" figure, and ±250 nm should be easily obtained. In Table 7-2 alignment tolerances are calculated for different scenarios using these assumptions. At present the mapping function is operational, and all wafers to be aligned in the future (both with this system and with the contact aligner used in this work) will be mapped.

For a stepper-based process flow and without special consideration given to integration requirements, it has been determined that wafer-to-wafer alignment accuracy is limited to approximately 130–180 nm (1σ) for wafers processed in our facility. Substrate temperature control during the alignment process is an essential requirement to achieve high accuracy. An in-situ wafer mapping capability has been

43

TABLE 7-1

Standard Deviations of Alignment Data Distributions

Pair Type and Axis	Metal-Only X Axis	Metal-Only Y Axis	Device X Axis	Device Y Axis
1σ (μm) corrected for translation and rotation	0.309	0.318	0.398	0.447
1σ (μm) corrected for translation, rotation, and scale	0.127	0.147	0.137	0.181

TABLE 7-2

Derived Alignment Tolerances

Assumptions	Alignment Tolerance	Via Pitch for 1-μm Via with 0.35-μm Metal Spacing
Best-case alignment with temperature control (Minimum 1σ + 0.125-μm alignment accuracy)	0.252	1.854
Worst-case alignment with temperature control (Maximum 3σ + 0.250-μm alignment accuracy)	0.793	2.936
Best-case alignment without temperature control (Minimum 1σ + 0.125-μm alignment accuracy)	0.434	2.218
Worst-case alignment without temperature control (Maximum 3σ + 0.250-μm alignment accuracy)	1.591	4.532

included in an alignment system currently under construction that will provide data to gain a greater understanding of the factors that dominate three-dimensional integration technology.

K. Warner C. K. Chen
R. D'Onofrio C. Keast
S. Poesse

REFERENCES

1. J. Burns, L. McIlrath, C. Keast, C. Lewis, A. Loomis, K. Warner, and P. Wyatt, *International Solid-State Circuits Conference Digest of Technical Papers* (IEEE, Piscataway, NJ, 2001), p. 268.

2. K. Warner, J. Burns, C. Keast, R. Kunz, D. Lennon, A. Loomis, W. Mowers, and D. Yost, *International SOI Conference Proceedings* (IEEE, Piscataway, NJ, 2002), p. 123.

3. Metra 2100 Process Engineer's Manual, Optical Specialties Inc., 1993.

4. P. Lindner, V. Dragoi, T. Glinsner, C. Schaefer, and R. Islam, *Electronic Components and Technology Conference Proceedings* (IEEE, Piscataway, NJ, 2002), p. 1439.

5. T. Itoh, K. Kataoka, and T. Suga, *International Conference on Solid-State Sensors and Actuators Digest of Technical Papers* (IEEE, Piscataway, NJ, 2001), p. 222.

REPORT DOCUMENTATION PAGE

1. REPORT DATE *(DD-MM-YYYY)*	2. REPORT TYPE	3. DATES COVERED *(From - To)*
15-11-2004	Quarterly Technical Report	1 August – 31 October 2004

4. TITLE AND SUBTITLE

Solid State Research

5a. CONTRACT NUMBER
F19628-00-C-0002

5b. GRANT NUMBER

5c. PROGRAM ELEMENT NUMBER

6. AUTHOR(S)

David C. Shaver

5d. PROJECT NUMBER
221

5e. TASK NUMBER
961

5f. WORK UNIT NUMBER

7. PERFORMING ORGANIZATION NAME(S) AND ADDRESS(ES)

Lincoln Laboratory, MIT
244 Wood Street
Lexington, MA 02420-9108

8. PERFORMING ORGANIZATION REPORT NUMBER

2004:4

9. SPONSORING / MONITORING AGENCY NAME(S) AND ADDRESS(ES)

HQ Air Force Materiel Command
AFMC/STSC
Wright-Patterson AFB, OH 45433-5001

10. SPONSOR/MONITOR'S ACRONYM(S)

11. SPONSOR/MONITOR'S REPORT NUMBER(S)
ESC-TR-2005-056

12. DISTRIBUTION / AVAILABILITY STATEMENT

Approved for public release; distribution is unlimited.

13. SUPPLEMENTARY NOTES
None

14. ABSTRACT

This report covers in detail the research work of the Solid State Division at Lincoln Laboratory for the period 1 August through 31 October 2004. The topics covered are Quantum Electronics, Electro-optical Materials and Devices, Submicrometer Technology, Biosensor and Molecular Technologies, Advanced Imaging Technology, Analog Device Technology, and Advanced Silicon Technology. Funding is provided by several DoD organizations—including the Air Force, Army, DARPA, MDA, Navy, NSA, and OSD—and also by the DOE, NASA, and NIST.

15. SUBJECT TERMS

quantum electronics	biosensor technology	semiconductor lasers	orthogonal-transfer arrays
electro-optical devices	molecular technology	heterostructure growth	chirp generation
materials research	advanced imaging technology	immersion lithography	IC fabrication
submicrometer technology	analog device technology	DNA analysis	

16. SECURITY CLASSIFICATION OF:			17. LIMITATION OF ABSTRACT	18. NUMBER OF PAGES	19a. NAME OF RESPONSIBLE PERSON
a. REPORT Unclassified	**b. ABSTRACT** Same as report	**c. THIS PAGE** Same as report	None	68	**19b. TELEPHONE NUMBER** *(include area code)*